

# A Catalog of Broad Absorption Line Quasars from the Sloan Digital Sky Survey Early Data Release

Timothy A. Reichard,<sup>1</sup> Gordon T. Richards,<sup>1,2</sup> Donald P. Schneider,<sup>1</sup> Patrick B. Hall,<sup>2,3</sup> Alin Tolea,<sup>4</sup> Julian H. Krolik,<sup>4</sup> Zlatan Tsvetanov,<sup>4</sup> Daniel E. Vanden Berk,<sup>5</sup> Donald G. York,<sup>6,7</sup> G.R. Knapp,<sup>2</sup> James E. Gunn,<sup>2</sup> and J. Brinkmann<sup>8</sup>

## ABSTRACT

We present a catalog of 224 broad absorption line quasars (BALQSOs) from the Sloan Digital Sky Survey's Early Data Release Quasar Catalog, including a relatively complete and homogeneous subsample of 131 BALQSOs. Since the identification of BALQSOs is subject to considerable systematic uncertainties, we attempt to create a complete sample of SDSS BALQSOs by combining the results of two automated selection algorithms and a by-eye classification scheme. One of these automated algorithms finds broad absorption line troughs by comparison with a composite quasar spectrum. We present the details of this algorithm and compare this method to that which uses a power-law fit to the continuum. The BALQSOs in our sample are further classified as high-ionization BALQSOs (HiBALs), low-ionization BALQSOs (LoBALs), and BALQSOs with excited iron absorption features (FeLoBALs); composite spectra of each type are presented. We further present a study of the properties of the BALQSOs in terms of the

---

<sup>1</sup>Department of Astronomy and Astrophysics, The Pennsylvania State University, 525 Davey Laboratory, University Park, PA 16802.

<sup>2</sup>Princeton University Observatory, Peyton Hall, Princeton, NJ 08544.

<sup>3</sup>Departamento de Astronomía y Astrofísica, Pontificia Universidad Católica de Chile, Casilla 306, Santiago 22, Chile.

<sup>4</sup>Department of Physics and Astronomy, The Johns Hopkins University, 3400 North Charles Street, Baltimore, MD 21218-2686.

<sup>5</sup>Department of Physics and Astronomy, University of Pittsburgh, 3941 O'Hara Street, Pittsburgh, PA 15260.

<sup>6</sup>Department of Astronomy and Astrophysics, The University of Chicago, 5640 South Ellis Avenue, Chicago, IL 60637.

<sup>7</sup>Enrico Fermi Institute, The University of Chicago, 5640 South Ellis Avenue, Chicago, IL 60637.

<sup>8</sup>Apache Point Observatory, P.O. Box 59, Sunspot, NM 88349.

balnicity distribution, which rises with decreasing balnicity. This distribution of balnicities suggests that the fraction of quasars with intrinsic outflows may be significantly underestimated.

*Subject headings:* quasars: general — quasars: absorption lines

## 1. Introduction

The nature of BALQSOs has been a question at the forefront of quasar research for the past two decades (Turnshek 1984; Weymann 1995), and considerable uncertainty remains about the nature of the absorption. One proposed explanation of the broad absorption line (BAL) phenomenon is that BALQSOs and nonBALQSOs are distinct populations of objects (Surdej & Hutsemekers 1987). Similarly some have argued that only LoBALs are a different class of quasars (Boroson & Meyers 1992), while others suggest that BALQSOs and nonBALQSOs are the same type of quasar but viewed from different orientations (Weymann et al. 1991; Ogle et al. 1999; Schmidt & Hines 1999) or at different stages in their life cycles (Becker et al. 2000).

Regardless of the nature of their hosts, it is clear that BAL troughs are caused by outflowing gas that is intrinsic to the quasar and are not produced by galaxies along the line of sight (as is the case for most narrow absorption systems). The traditional definition of a BAL trough requires that the outflows extend to considerable velocities from the quasar’s emission redshift; however, it is possible that these intrinsic outflows extend to smaller velocities and are related to the so-called “associated” absorbers that are not as broad and have smaller terminal velocities (Foltz et al. 1986). Some of these associated systems are known to be intrinsic outflows, but others may simply be the result of absorption in the host galaxy or a nearby galaxy.

The characteristics of BALQSOs have been the subject of a number of previous studies. Working from the Large Bright Quasar Survey (LBQS; Hewett, Foltz, & Chaffee 1995), Weymann et al. (1991) compiled the largest previous BALQSO sample. They found that, after approximately correcting for selection effects, BALs occurred in  $\simeq 12\%$  of all quasars, but with a striking lack of BALs in radio-loud quasars. They also created composite spectra for both BAL and “normal” quasars, using 42 nonBALQSOs and 40 BALQSOs, including 6 low-ionization BALQSOs (LoBALs) and 34 high-ionization BALQSOs (HiBALs). More recently Brotherton et al. (2001) created composite BALQSO spectra using 25 HiBALs and 18 LoBALs from the FIRST Bright Quasar Survey (FBQS; White et al. 2000).

The Sloan Digital Sky Survey (SDSS; York et al. 2000) will produce a sample of quasars

that is more than 100 times larger than either the LBQS or FBQS, and the SDSS should be relatively unbiased with respect to BALQSOs. Already, Menou et al. (2001) have examined 13 radio-detected SDSS/FIRST quasars with BAL-like intrinsic absorption. The properties of the most extreme cases of SDSS BALQSOs have been presented by Hall et al. (2002). Tolea, Krolik, & Tsvetanov (2002) discussed the principal statistical properties of a sample of C IV BALs drawn from a restricted subset of the EDR quasars studied herein.

The size of the sample of BALQSOs produced by the SDSS suggests that the time is ripe to explore new methods for identifying outflows in AGN. Hall et al. (2002) have suggested a modification for the classification of BALQSOs that imposes less restrictive constraints on the extent of the absorption in BALQSOs. Herein, we explore a different method of determining the underlying continuum and emission line flux, and compare the results with the standard BAL approach as was used by Tolea et al. (2002).

Thus, the primary goals of this new paper are three-fold: (1) the comparison of our composite based continuum+emission line fitting procedure with the traditional power-law continuum plus Gaussian emission line fitting procedure for defining BALQSOs, (2) the construction of a large, well-defined sample of BALQSOs, and (3) the presentation of the resulting distribution of balnicity indices for BALQSOs.

The paper by Tolea et al. (2002) and this paper differ in a number of ways including (1) the definition of the underlying continuum+emission, (2) the way the sample is restricted in order to produce a more homogeneous sample, and (3) the selection and classification of LoBALs. In this paper we will compare and contrast our results to Tolea et al. (2002) and show that the two methods/samples produce similar results. A detailed investigation of the continuum and emission line properties of these BALQSOs will be presented by Reichard et al. (2003). We reserve detailed discussion of the BAL fraction as a function of redshift to Reichard et al. (2003) since there are color dependent selection effects that must be considered.

In § 2 we define our quasar sample. A discussion of the process by which we fit individual spectra to a composite spectrum to define the intrinsic flux level is given in § 3. Our method of classifying quasars into nonBAL, HiBAL, LoBAL, and FeLoBAL subsamples can be found in § 4, which also presents our BALQSO catalog and composite spectra of our subsamples. The catalog has two parts: a relatively complete subsample of BALQSOs that meet the traditional BALQSO definition (nonzero balnicity index) and lie within the redshift range  $1.7 \leq z \leq 4.2$ , and a supplementary listing of BALQSOs largely outside this redshift range. Using our BALQSO catalog, we discuss the balnicity index distribution in §5; §6 summarizes our results. Throughout this paper we will use the cosmology that is traditionally used to define quasar luminosities, where  $H_o = 50 \text{ km s}^{-1} \text{ Mpc}^{-1}$ ,  $\Omega_M = 1$ , and  $\Omega_\Lambda = 0$ . We also

adopt a convention for optical spectral index such that  $\alpha = \alpha_\lambda$  unless stated otherwise, where  $f_\lambda \propto \lambda^{\alpha_\lambda}$ .

## 2. The Data

The parent sample for our investigation of BALQSOs consists of the 3814 bona fide quasars ( $M_{i^*} < -23$ , with at least one line broader than  $1000 \text{ km s}^{-1}$ ) from the SDSS Early Data Release (EDR; Stoughton et al. 2002) quasar catalog (Schneider et al. 2002). These quasars were selected for spectroscopic follow-up from the SDSS imaging survey, which uses a wide-field multi-CCD camera (Gunn et al. 1998). The spectra cover the optical range  $3800\text{--}9200 \text{ \AA}$  at a resolution of  $1800\text{--}2100$ . As discussed by Stoughton et al. (2002), quasar candidates were identified using three different preliminary versions of the SDSS Quasar Target Selection Algorithm (Richards et al. 2002a), which identifies quasar candidates according to their broad-band SDSS colors (Fukugita et al. 1996; Stoughton et al. 2002). EDR quasars were also identified as optical matches to both radio sources from the VLA “FIRST” survey (Becker, White, & Helfand 1995) and *ROSAT* All-Sky Survey (Voges et al. 1999) sources and also as “serendipitous” sources (see § 4.8.4.3 in Stoughton et al. 2002). Details of the SDSS photometric calibrations are given by Hogg et al. (2001) and Smith et al. (2002), and the astrometric calibration is described by Pier et al. (2002). The spectroscopic tiling algorithm is discussed by Blanton et al. (2002).

Although the quasar selection algorithm has been evolving, the differences between the EDR versions of quasar target selection (Stoughton et al. 2002) and the final version of quasar target selection Richards et al. (2002a) are largely for quasars with  $z \sim 3.5$  and  $z \sim 4.5$ . Thus the BALQSOs studied herein should be representative of the BALQSOs that will be discovered as part of the final, homogeneous SDSS quasar survey (at least for those quasars with  $i^* < 19.1$  — the SDSS quasar target selection magnitude limit; in the present study we also include some fainter quasars from the EDR quasar sample that were selected to fainter limits). In order to define a more homogeneously selected sample, we have also indicated which of the BALQSOs presented in this catalog would have been selected using the final SDSS quasar selection algorithm presented by Richards et al. (2002a).

### 3. Composite Spectra Fitting

#### 3.1. Overview

Determining whether a quasar is a BALQSO is a complicated task. The standard method is to calculate the “balnicity” index (BI), defined by Weymann et al. (1991).<sup>9</sup> A BI of zero indicates that broad absorption is absent, while a positive BI indicates not only the presence of one or more broad absorption troughs, but also the amount of absorption. However, the Weymann et al. (1991) definition is not free of complications; specifically, how does one define the true continuum+emission line level and the systemic redshift when there is significant absorption? Broad absorption lines remove flux from the blue wing of emission lines, thus the flux level from which to measure absorption is not the continuum alone, but must also include emission line flux.

To measure BIs in our BALQSO sample, we used two largely automated methods. One of the automated schemes is described in Tolea et al. (2002). The other is new, and so we describe it in detail here.

In previous studies, the general procedure has been to approximate the continuum by a selected analytic form (usually a power-law) and fit it to the spectrum, avoiding (to the degree possible) those portions with strong line features, whether emission or absorption. The emission line corresponding to BAL features is modeled by mirror-imaging the profile of the red wing onto the blue side about either the measured or expected peak of C IV. This is essentially the process that was used by Tolea et al. (2002) to measure balnicity indices in their BALQSO sample of 116 objects. Although this process works relatively well, the overall similarity of quasar spectra combined with issues such as emission line blueshifts and asymmetries suggest that a template fitting procedure might work as well as the traditional method. Thus we have developed an automated procedure based on fitting to a template quasar spectrum; we will compare the results of this process to the more traditional method.

From Richards et al. (2001) and Vanden Berk et al. (2001), we know that quasars at a given redshift are very similar in the UV/optical part of the spectrum. Although there are

---

<sup>9</sup>The BI is essentially a modified equivalent width in velocity space and is defined as follows. Absorption between 3000 and 25000 km s<sup>-1</sup> blueward of C IV emission redshift is integrated so long as the absorption falls at least 10% below the continuum for at least 2000 km s<sup>-1</sup>. The 25000 km s<sup>-1</sup> limit is chosen to avoid emission and absorption from Si IV. Any absorption within 3000 km s<sup>-1</sup> and that fails to span at least 2000 km s<sup>-1</sup> in width is excluded in order to avoid contamination from absorption that might not be due to an outflow, specifically the so-called “associated” absorption lines (Foltz et al. 1986). BIs can range from 0 to 20000 km s<sup>-1</sup>.

small differences in the continuum slope and the strength of the emission lines, and there is a small fraction (few percent) of anomalously red quasars in the SDSS magnitude range (Richards et al. 2003), the average quasar spectrum is quite representative of the sample as a whole. On the basis of this perceived similarity of different quasar spectra, we chose to use the EDR composite quasar spectrum to define the continuum and emission line levels for our balnicity index determinations in this new composite-based method. The EDR composite quasar spectrum was created in the same manner as the Vanden Berk et al. (2001) quasar composite spectrum, but using only the 3814 EDR quasars; note that BALQSOs have not been removed from the EDR composite quasar spectrum — by definition.

We model the true continuum and emission line levels for a quasar with unknown properties by fitting the EDR composite quasar spectrum to the input spectrum that we wish to check for BAL troughs. In matching the composite quasar spectrum to the input spectrum, we must allow for changes in the slope and shape of the continuum between the input quasar spectrum and the template quasar spectrum. We adjust the overall slope by multiplying by a power-law; we model additional spectral “curvature” relative to the composite in terms of dust extinction. We now turn to a discussion of these issues.

### 3.2. Dust Reddening Laws

To allow for changes in the shape of the continuum, we make use of a dust reddening law with color excess (reddening),  $E(B - V)$ , as a parameter in our fits. Dust reddening is a function of wavelength, and reddening by dust will introduce curvature into an otherwise power-law continuum. We emphasize that there is no a priori reason to require that the curvature in a spectrum be caused by dust; however, there is growing evidence that BALQSOs can be dust reddened (e.g., Sprayberry & Foltz 1992; Yamamoto & Vansevicius 1999; Brotherton et al. 2001; Hall et al. 2002). Still, it could be that any curvature or apparent reddening in the spectrum of a quasar is caused by processes other than dust; we will elaborate on this issue more in Reichard et al. (2003).

For our present purposes, however, we will assume that the cause of any curvature in the spectrum of a quasar relative to the composite is due to dust reddening (and extinction). We will determine the amount of “reddening” and power-law spectral index adjustment by simultaneously fitting for both parameters. To simplify the process, we will assume that any dust reddening is located at the quasar redshift and is not caused by dust exterior to the quasar along our line of sight. If the reddening instead occurs primarily along the line of sight, it will simply change the resulting values of  $E(B - V)$ , but will not significantly change the amount of curvature in the spectrum.

A review of the extinction due to dust is given by Savage & Mathis (1979); see also Mihalas & Binney (1981). The extinction, typically written as  $A_\lambda$  at a given wavelength,  $\lambda$ , is given by

$$A_\lambda = E(\lambda - V) + R_V \times E(B - V), \quad (1)$$

where  $E(\lambda - V) \equiv A_\lambda - A_V$  is the color excess. The observed extinction laws typically have an approximately  $\lambda^{-1}$  dependence, but there are differences among the extinction laws for the Milky Way (Cardelli, Clayton, & Mathis 1989), the Large Magellanic Cloud (LMC; Nandy et al. 1981), and the Small Magellanic Cloud (SMC; Prevot et al. 1984). The main differences are the relative slopes of the extinction as functions of  $\lambda$  and the strength of the so-called “2200 Å bump”; see Sprayberry & Foltz (1992).

For most extragalactic sources, including quasars, the 2200 Å bump is either weak or missing, and the SMC reddening law is often assumed to be the most appropriate law to use (it has the weakest 2200 Å bump). Throughout this paper we will use the SMC extinction curve as given by Pei (1992), which has  $R_V = 2.93$  and goes roughly as  $\lambda^{-1}$  in the UV/optical part of the spectrum that is covered by our spectra.

### 3.3. Continuum Adjustment

During the process of adjusting the continuum of the composite spectrum to match each input spectrum, we assume that the quasar continua follow a power-law relation that is diminished by dust extinction characterized by the color excess  $E \equiv E(B - V)$  using the Pei (1992) SMC reddening law. We begin by expressing a spectrum as

$$f(\lambda; \alpha, E) \propto \lambda^\alpha 10^{-aE\xi(\lambda)}, \quad (2)$$

where  $a = 0.4(1 + R_V)$ ,  $\xi(\lambda)$  is the extinction curve as given by Pei (1992), and rest wavelengths,  $\lambda$ , are given in microns. We determine the spectral index,  $\alpha$  ( $= \alpha_\lambda = -2 - \alpha_\nu$ ), and reddening,  $E$ , of each input spectrum by fitting to each an adjusted composite spectrum. The composite spectrum  $f_c(\lambda; \alpha_c, E_c)$  is adjusted to  $f'_c(\lambda; \alpha, E)$  by changing its spectral index and reddening using

$$f'_c(\lambda; \alpha, E) = f_c(\lambda; \alpha_c, E_c) \lambda^{(\alpha - \alpha_c)} 10^{-a(E - E_c)\xi(\lambda)}. \quad (3)$$

We fit the composite spectrum to each input spectrum by minimizing a weighted  $\chi^2$  function. Minimization is more easily achieved by smoothing the input spectra before evaluating the  $\chi^2$  function, and so we smooth by 15 pixels. Expressing an adjusted composite spectrum as  $f'_c(\lambda; \alpha, E)$  and a smoothed input spectrum as  $f_i(\lambda; \alpha_i, E_i)$  with error spectrum  $\sigma_i(\lambda)$ , we

find the values of  $\alpha$  and  $E$  that minimize the  $\chi^2$  function

$$\chi^2(\alpha, E) = \frac{\sum_{\lambda} \left( \frac{f'_c(\lambda; \alpha, E) - f_i(\lambda; \alpha_i, E_i)}{\sigma_i(\lambda)} \right)^2 w(\lambda)}{\sum_{\lambda} w(\lambda)}. \quad (4)$$

The weight function  $w(\lambda)$  is used to remove or reduce the effects of prominent emission lines. The emission line regions excised are the lower and upper wavelength limits given by Vanden Berk et al. (2001) for Ly $\alpha$ +N V, Si IV, C IV, C III], and Mg II. The other excluded and deweighted regions are the C IV broad absorption line region (inclusive from the Si IV emission line peak to the C IV peak), the Mg II broad absorption line region (from  $\lambda 2575 \text{ \AA}$  to  $\lambda 2686 \text{ \AA}$ ), the Lyman- $\alpha$  forest (shortward of  $\lambda 1050 \text{ \AA}$ ), and wavelengths redward of  $4150 \text{ \AA}$  (the longest wavelength at which the composite spectrum matches a power law continuum line, as shown in Figure 6 of Vanden Berk et al. 2001). For a pixel in one of the broad absorption regions,  $w(\lambda) = 0.5$ ; in one of these other excluded wavelength ranges,  $w(\lambda) = 0$ ; otherwise,  $w(\lambda) = 1$ . These regions are depicted in the bottom panel of Figure 1. The weight function ensures that the continua of the composite and input spectra are matched without having emission and absorption regions affecting the spectral index and reddening determinations. Although we would like to completely discount the broad absorption regions during the fitting process, fits are improved by giving the regions a lower, nonzero weight where the broad absorption region is the bluest accessible part of the spectrum. For example, in fitting the composite spectrum to compute a C IV balnicity index for an object with  $z \sim 1.70$ , the C IV broad absorption region must be given some weight; otherwise, little of the spectrum blueward of the red tail of the C IV emission line is counted, and the fitted composite may diverge blueward of the emission line.

Before the  $\chi^2$  function is evaluated, the adjusted composite spectrum is normalized to match the average flux density of the input spectrum in a small wavelength range. We chose different normalization windows when defining a continuum for C IV and Mg II balnicity indices:  $1725 \pm 25 \text{ \AA}$  for C IV ( $1.7 \leq z \leq 4.2$ ), and  $3150 \pm 25 \text{ \AA}$  ( $0.5 \leq z \leq 1.9$ ) and  $2200 \pm 25 \text{ \AA}$  ( $1.9 < z \leq 2.1$ ) for Mg II. The  $3150 \text{ \AA}$  window is preferred for computing Mg II balnicity indices because of its close proximity to the Mg II emission line, but it is redshifted beyond the ends of the good spectral range for SDSS spectra with redshifts greater than  $\sim 1.9$ . We choose  $2200 \text{ \AA}$  for higher redshifts ( $1.9 < z \leq 2.1$ ) for which the Mg II absorption region remains in the spectral range. These values are chosen to be in wavelength ranges that are accessible for all of the objects in the redshifted wavelength ranges considered and that are reasonable local continua (i.e., not affected by strong emission or absorption lines); see §4.

The  $\chi^2$  function is minimized by employing a modified Newton-Raphson method (Press



et al. 1992), which quadratically converges to the values of  $\alpha$  and  $E$  that minimize the function. Using  $\alpha = \alpha_c$  and  $E = E_c$  as initial guesses yields a convergence fraction of 92%. When convergence succeeds, the  $\chi^2$  function is evaluated at points  $(\alpha, E)$  close to the convergence point  $(\alpha_i, E_i)$ , and the convergence point is adjusted as necessary if a new local minimum is found. When convergence fails, we evaluate the  $\chi^2$  function over a wide grid of  $(\alpha, E)$  points and choose the minimizing values. Despite the simplicity of this latter approach, we prefer the Newton-Raphson method as the primary method because of its fast convergence.

Examples of the results of this procedure are shown in Figure 1. Here we show the continuum-adjusted composite quasar spectra (gray line) over-plotted on a sample non-BALQSO (top panel) and three HiBALs (middle three panels). The C IV emission lines of the EDR composite spectrum have been scaled to match the peak line flux of the objects; see §3.6. The spectra are normalized at the redshifted wavelength  $1725(1+z)$  Å.

### 3.4. Goodness of Fit Analysis

The quality of the fits can be measured by reduced  $\chi^2$  (which we call  $\chi_\nu^2$ ), the total  $\chi^2$  divided by the number of degrees of freedom. The distribution of this quantity is shown in Figure 2. For the number of degrees of freedom in our fitting scheme ( $\sim 10^3$ ; the actual number varies over a range of a factor of 3 for different objects), fits would ordinarily be deemed acceptable only if  $\chi_\nu^2$  is at most slightly greater than unity. None of our fits meets this test.

On the other hand, 90% yield  $\chi_\nu^2$  values  $\leq 2.5$ . For several reasons, we consider fits this good to be acceptable *for our purposes*. First of all, we are not claiming physicality for the parameters (e.g., extinction) that we infer; all we really need is a reasonable description of the flux before absorption in the vicinity of the C IV and Mg II lines. Second, we are not computing  $\chi^2$  in strictly the standard sense since we weight some regions of the spectrum differently than others. Third, we are deliberately not modeling certain features that can add to  $\chi^2$ , such as intervening Ly $\alpha$  absorption and, of course, BAL absorption. Fourth, we are compelled to make use of a wavelength band near 1300 Å which we know to be contaminated by a variable amount of emission line flux that we do not model. Including this band is necessary because fixing the global continuum shape across the C IV region requires fitting to some region blueward of that feature, and this band is the *least* contaminated band available.

When  $\chi_\nu^2 > 2.5$ , we visually inspected the spectra in order to attempt an improvement.

If we believed that the fit in the C IV region was reasonable (no matter what departures occurred elsewhere), we accepted the fit, otherwise a new fit with zero extinction was constructed. If that resulted in an improved description of the C IV region, we accepted the new fit. If it did not, we marked that object as having an unmeasurable balnicity. Interestingly, every quasar falling into this last category turned out to be an FeLoBAL.

In Figure 2 we show the distribution of  $\chi^2_\nu$  for all of the quasars in the redshift range that we have searched for BAL troughs (solid line). The dashed line gives the distribution for BALQSOs. Note that the distribution for BALQSOs is skewed towards slightly larger values — as expected; absorption features, by definition, will not match the continuum as defined by the composite spectra and will contribute to an increase in  $\chi^2$ . However, the similarity of the two distributions shows that BALs by themselves are not the major contributor to  $\chi^2$ .

### 3.5. Degeneracy of Spectral Index and Reddening

It is perhaps not surprising that several combinations of the two fit parameters (spectral index and reddening) produce satisfactory fits. This result originates from the nature of the  $\chi^2(\alpha, E)$  function. Figure 3 shows a typical contour plot of the paraboloid-like surface generated by the reduced  $\chi^2$  distribution. The surface is quite smooth and has a clear valley along a line  $\Delta\alpha = \beta E$ , where  $\Delta\alpha \equiv \alpha - \alpha_0$  and  $\beta \sim -10$  is the tradeoff between spectral index and reddening.<sup>10</sup> This line has a small positive concavity and hence a local surface minimum at the minimizing spectral index and reddening. Although in principle this local minimum represents the best-fit parameters, the small curvature of the valley line allows nearby points on this line to function, as well as the local minimum, as best-fit parameters. More specifically, small changes in the fit parameters from the local minimum leave the reduced  $\chi^2$  value nearly unchanged.

Deviations on the order of  $\delta\alpha = \pm 0.10$  and  $\delta E = \mp 0.010$  ( $= \delta\alpha/\beta$ ) produce a typical change in reduced  $\chi^2$  of  $< 0.01$ . For example, for the quasar SDSS J003019.82–002602.6, the minimum was found near  $(\alpha, E, \chi^2_\nu) = (-1.99, 0.055, 1.105)$ , but the nearby point  $(-1.90, 0.046, 1.107)$  is reasonably as good a fit (the corresponding probability changes from 0.860 to 0.865).

The tradeoff between spectral index and reddening results from a combination of the wavelength range included in the  $\chi^2$  function (where  $w(\lambda) > 0$ ) and the normalization wavelength. This can be shown by equating a power law with spectral index  $\alpha_0$  to an SMC-reddened power law with spectral index  $\alpha$  and reddening  $E$  and solving for the tradeoff.

---

<sup>10</sup>We use spectral indices in  $\lambda$ -space. In  $\nu$ -space,  $\Delta\alpha_\nu = -\Delta\alpha_\lambda$ , and  $\beta$  will change sign accordingly.

Upon normalizing both the power law and reddened power law to unity at  $\lambda_0$ , the tradeoff (using a power-law approximation to the SMC reddening law with exponent,  $D = 1.2$  and  $a = 1.39$ ) is

$$\frac{\Delta\alpha}{E} = \left( \frac{1}{\lambda^D} - \frac{1}{\lambda_0^D} \right) \frac{a}{\log_{10}(\lambda/\lambda_0)}. \quad (5)$$

We can take the arithmetic mean (via integration) of the tradeoff over a wavelength range  $\lambda_1 < \lambda < \lambda_2$  that includes the C IV and Mg II emission lines. This yields the average tradeoff

$$\beta \equiv (\lambda_2 - \lambda_1)^{-1} \int_{\lambda_1}^{\lambda_2} \frac{\Delta\alpha}{E} d\lambda. \quad (6)$$

The average tradeoff remains a function of the normalization wavelength  $\lambda_0$ . Integrating over  $1500 \text{ \AA} < \lambda < 3200 \text{ \AA}$ ,  $\beta$  is nearly linear in the same range of  $\lambda_0$ , as shown in the inset of Figure 4. We use three normalization points at  $1725 \text{ \AA}$ ,  $2200 \text{ \AA}$ , and  $3150 \text{ \AA}$ , and the corresponding tradeoffs are  $-10.8$ ,  $-9.3$ , and  $-7.6$ , respectively. Thus when the composite-fitting algorithm fails to converge to the best-fitting spectral index and reddening values, a simple power law with spectral index  $\alpha_0$  can be fitted to the curve. Then a new initial guess of spectral index  $\alpha$  and reddening  $E = (\alpha - \alpha_0)/\beta$  can be tried to promote convergence.

Figure 4 illustrates how changing the the spectral index of a power law and the reddening can mimic the original power law. We have plotted a pure power law with  $\alpha = -1$  (*thick solid line*). To recover this red power law by using a blue power law with  $\alpha = -2$  (*thick dashed line*), the blue power law is reddened by an amount determined by the tradeoff. SMC-reddened power laws with  $E(B - V) = 0.091, 0.100$ , and  $0.111$ , corresponding to  $\beta = \Delta\alpha/E = -11, -10$ , and  $-9$ , are over-plotted in thin long-dashed, short-dashed, and dotted lines, respectively. All of the curves are normalized to unity at  $1725 \text{ \AA}$ .

In sum, although we regard our fits as providing a reasonable description of the spectral shape, the best-fit parameters should not be taken as physical — these are *not* genuine measurements of extinction; for this reason, we do not list them in our catalog. However, even though the absolute values are not physical, the relative values may still be meaningful; this possibility will be explored in Reichard et al. (2003) when we study the continuum properties of BALQSOs in more detail.

### 3.6. Emission Line Peak Adjustment

Although the average quasar spectrum is representative of the whole EDR quasar sample, in addition to differences in the slope and shape of the continuum between individual quasars, there are also differences in the emission line regions. Since we are using the average quasar spectrum as our template continuum+emission spectrum, we must adjust this

template in the emission line regions when the strength of the emission lines in the template does not match the strength in an individual quasar. Fortunately, the equivalent width distribution of broad lines in quasars spans only a factor of  $\sim 10$ , whereas the luminosity of quasars spans a few orders of magnitude.

To improve the fitted composite spectrum as a continuum for balnicity index measurement, we scale the C IV and Mg II emission lines to match the peak flux density of the input spectrum. The process is straightforward: after the composite is adjusted by the fitting process described in § 3.3, the normalized, reddened power law that is the result of that fitting is subtracted from both the adjusted composite and the input spectra; we then multiply the composite flux density in the emission line region by the ratio of the peak flux densities in the line; and re-add the normalized, reddened power law. This method has the virtue of automatically shifting the C IV line center relative to the other emission line centers and also giving its profile the mean asymmetry since the SDSS determines redshifts using empirical instead of laboratory wavelengths for emission lines. For example, in the mean C IV is shifted  $\simeq 800 \text{ km s}^{-1}$  blueward of Mg II (Richards et al. 2002b) and  $340 \text{ km s}^{-1}$  blueward of C III] (Vanden Berk et al. 2001).

Although this process yields line profiles that appear to be in reasonably good agreement with the data, this approach is not perfect and one can imagine better ways of adjusting the emission line strengths. In, particular, it is known that the strength of the C IV emission line is dependent upon the luminosity of the quasar (Baldwin 1977; Osmer, Porter, & Green 1994) and the velocity offset of the C IV peak with respect to Mg II (Richards et al. 2002b). In addition, in the composite method we make no allowance for any variation in either the width of the C IV line or its shift relative to line-center as found in the composite, even though both can vary considerably from quasar to quasar (e.g., Wilkes 1986). Note that more conventional methods (e.g., Tolea et al. 2002) fit the width of the C IV line but assume its line-center is at the same redshift as some standard (e.g., C III]1909), which may be shifted from systemic. In the future, we hope to account for emission line differences by having not just one, but many template spectra.

## 4. BALQSO Catalog

### 4.1. Balnicity Determination and Sample Definitions

Once an intrinsic spectral shape has been chosen by our fitted composite spectrum method, the balnicity of the input spectrum can be determined. Balnicity indices are computed for two lines: C IV and Mg II. The algorithm was applied to each EDR quasar

spectrum, measuring the properties of any absorption troughs, i.e., determining if each spectrum is a HiBAL (broad absorption trough just blueward of C IV emission), a LoBAL (broad absorption troughs just blueward of both the C IV and Mg II emission lines — but other lines such as Al III could be used as well), or a nonBAL (no broad absorption troughs just blueward of the C IV and Mg II emission lines). The C IV balnicity index uses the traditional (Weymann et al. 1991) definition, and the Mg II balnicity index is a modified version (see below). Hall et al. (2002) discuss how the determination of balnicity indices might be improved in the future.

The fixed observed wavelength coverage of the SDSS EDR spectra ( $3800 \text{ \AA} \leq \lambda \leq 9200 \text{ \AA}$ ) imposes constraints on the redshifts at which BALQSOs can be identified and at which balnicity indices can be calculated in our automated fashion. First, for this catalog we restrict ourselves to identifying as BALQSOs those quasars with C IV absorption at least  $2000 \text{ km s}^{-1}$  broad located between  $3000$  and  $25,000 \text{ km s}^{-1}$  blueward of the quasar redshift (or Mg II absorption  $1000 \text{ km s}^{-1}$  broad between  $0$  and  $25,000 \text{ km s}^{-1}$  blueward of the quasar redshift; see below). Second, complete samples of BALQSOs can be identified only for redshifts at which the EDR spectra contain the entire  $25,000 \text{ km s}^{-1}$  range which is searched for BAL troughs.<sup>11</sup> Third, for our automated balnicity index calculation, the redshifts must be restricted so that the normalization windows at  $1725 \text{ \AA}$  (for C IV) and  $3150 \text{ \AA}$  (for Mg II) are observed. These constraints restrict the redshift range to  $1.7 \leq z \leq 4.2$  for C IV and  $0.5 \leq z \leq 1.9$  for Mg II. We can extend this latter range to  $0.5 \leq z \leq 2.1$  by normalizing at  $2200 \text{ \AA}$  for  $z > 1.9$ . BALQSOs with redshifts outside of these ranges can also be identified, but not in a complete sense.

We modified our Mg II balnicity index definition from the C IV definition in two ways. Mg II broad absorption troughs tend to be weaker and narrower than those found in C IV troughs (Voit, Weymann, & Korista 1993). The minimum Mg II continuous absorption width was chosen to be  $1000 \text{ km s}^{-1}$ . Moreover, the Mg II absorption removes flux density at smaller velocity displacements (on average) from the center of the emission line than is the case in C IV. We accordingly adjust the minimum velocity from  $3000 \text{ km s}^{-1}$  to  $0$  to include low-velocity absorption in the Mg II balnicity index (see Hall et al. 2002 for further justification of these modifications). The Mg II balnicity indices were computed in the same manner as for C IV balnicity indices but with normalization at  $3150 \text{ \AA}$  or  $2200 \text{ \AA}$  (depending on the quasar redshift).

Since all known quasars that exhibit low-ionization BAL troughs also exhibit high-

---

<sup>11</sup>These samples could still be slightly incomplete, as BAL troughs are known to exist at higher outflow velocities.

ionization BAL troughs, we limited our Mg II BALQSO sample to objects that we have identified as C IV BALQSOs and those objects with redshifts  $0.5 \leq z \leq 1.7$  whose C IV balnicity index cannot be computed. Our HiBAL sample will be broken into subsamples including and excluding LoBALs. Note that our semi-automated algorithm does not make an attempt to classify objects as LoBALs based on Al III absorption. Since Al III absorption can be stronger than Mg II absorption in LoBALs, our method will miss some fraction of the LoBALs. However, our by-eye classification should have recovered most of those Al III LoBALs missed by our semi-automated algorithm.

## 4.2. Construction of the Catalog

C IV BALQSOs were selected from the EDR sample first by choosing those objects with a non-zero balnicity index as determined by either the composite method, the method of Tolea et al. (2002), or visual inspection by one of us (PBH). The two automated methods selected very nearly the same objects over their common redshift range. Spectra of each of these BALQSO candidates were then inspected by eye.

A small number of objects were discarded from the initial composite-generated BALQSO list because the composite spectrum continuum poorly matched the object’s continuum, and the balnicity calculation was suspect. The poor quality of the fit of the composite was typically the result of one of three causes. First, a few objects had extraneous emission or absorption at the normalization wavelength that shifted the fitted composite spectrum above or below the object spectra. NonBALQSOs with a high normalization will appear to have nonzero balnicity indices. Second, the  $\chi^2$ -minimization and  $(\alpha, E)$  point-scanning algorithms failed on some spectra that either had sufficiently strong absorption that a power law is not descriptive of the continuum, e.g., FeLoBALs, or the algorithms simply did not find a minimizing pair of fit parameters. These objects were reclassified by inspection as BALQSOs or nonBALQSOs. Third, a few objects with  $z \sim 1.7$  had excellent composite fits redward of the C IV emission line but with an overestimated continuum in the C IV broad absorption region, mainly because little of the weighted wavelength ranges were observed in these spectra blueward of the broad absorption region. We replaced these composite fits (fitted with the combination SMC reddening law and power law) with a composite fitted using a power law without reddening, recomputed the balnicity index, and reclassified the object. These three errors were more prominent in computing Mg II balnicity index, so we classified quasars as LoBALs only after visual inspection rather than relying solely on measured Mg II balnicity indices.

We present a complete catalog of BALQSOs from the EDR in the redshift range  $1.7 \leq$

$z \leq 4.2$  in Table 1. The BAL catalog consists of 185 BALQSOs, including 153 HiBALs, 24 LoBALs, and 8 FeLoBALs. Note that we include six quasars in Table 1 that formally have BI=0 (or where the BI is not measured). Three of them are LoBALs or FeLoBALs and should clearly be included. The three HiBALs should be excluded if a pure sample defined strictly using the Weymann et al. (1991) BI criteria is desired, but we believe that they should be included because they show troughs that came very near to satisfying the balnicity criteria. For example, there is a clear C IV absorption trough in SDSS 110838.76–005533.7, but it extends to a velocity larger than  $v = 25,000 \text{ km s}^{-1}$ , which throws off the automated fit.

In Table 1, column 1 lists the object names using the SDSS format of J2000 right ascension (hhmmss.ss) and declination ( $\pm$ ddmmss.s). Columns 2–4 list the plate, fiber, and modified Julian date. Columns 5–7 indicate whether an object was identified as a quasar candidate by the final version of the quasar target selection algorithm (Column 5, Richards et al. 2002a), by the EDR quasar target selection algorithm (Column 6), and by the EDR serendipity target selection algorithm (Column 7). Of the 185 BALQSOs in Table 1, Column 5 indicates that 131 of them meet the SDSS’s adopted quasar target selection criteria and thus constitute a more homogeneous subsample. Column 8 gives the FIRST peak flux density at 20 cm; 16 of our BALQSOs are radio-detected, only three of which overlap with Menou et al. (2001). A zero in this column means that the object is undetected in the FIRST survey at the  $\sim 1 \text{ mJy}$  limit; no data indicates that there is no FIRST observation at this location. Columns 9, 10 and 11 list the redshift, the apparent  $i^*$  magnitude (corrected for Galactic reddening; Schlegel, Finkbeiner, & Davis 1998) and the resulting absolute  $i^*$  magnitude, respectively. Columns 12–14 list the balnicity indices as follows: Columns 12 and 14 list C IV and Mg II balnicity indices computed by the composite-fitting algorithm (this paper), while Column 13 gives the C IV balnicity index as computed by using the traditional method by Tolea et al. (2002) for objects with  $1.8 \leq z \leq 3.8$ .

The subsequent four columns show the classification of the objects. Column 15 gives the classification according to our fitted composite algorithm: H = HiBAL and N = nonBAL. Column 16 shows the classification according to Tolea et al. (2002). All of the objects are labeled in this column as either “H” or “N” with similar meanings to those in Column 15. The two automated algorithms define continua in different ways. Because the continua are not identical, there are cases where they disagree on whether an object is a BALQSO. In the catalog we include all quasars defined as BALQSOs by either algorithm.

One of us (PBH) examined all of the EDR spectra for BALQSOs by eye; the resulting classifications are listed in Column 17. The following abbreviations are used: “HiZ” = HiBAL at  $z \geq 3.90$ , where LoBALs could be missed because  $\lambda_{\text{AIII}} > 9150 \text{ \AA}$ ; “HiZ/Loz” = Hi/LoBAL at  $z \geq 2.26$ , where LoBALs could be missed because  $\lambda_{\text{MgII}} > 9150 \text{ \AA}$ ; “Hi” =

only high-ionization lines are present; “Lo” = both high- and low-ionization lines are present; “LoZ” = LoBAL at  $z \geq 3.90$ , where LoBALs could be missed because  $\lambda_{\text{AIII}} > 9150 \text{ \AA}$ , “FeLo” = high-, low-, and metastable Fe II/Fe III lines ( $\sim 2600 \text{ \AA}$ , or otherwise) or atypical absorption that more readily classifies the object as an unusual or extreme BALQSO, usually with strong iron absorption; and “no” = no broad absorption lines are present (nonBAL). A question mark “?” means uncertainty in the previous code; e.g., “HiLo?” means a tentative LoBAL trough in a definite HiBAL.

Finally, Column 18 gives the overall classification upon which we have decided for each quasar. It lists an object as a LoBAL (“Lo”) if visual inspection classified the object as a LoBAL. Visual inspection also revealed a few unusual LoBALs with iron absorption (FeLoBALs), which are labeled instead by “FeLo”. The remaining objects are those classified as HiBALs by at least one of the three classification methods and are labeled “Hi”. We have supplied Mg II balnicity indices only for those objects classified as LoBALs in the redshift range  $0.5 \leq z \leq 2.1$

We also present a supplementary catalog of BALQSOs with redshift generally outside the range  $1.7 \leq z \leq 4.2$  in Table 2, but with absorption clearly broad enough to be considered as BALQSOs; the format is the same format as in Table 1. The supplement contains 39 BALQSOs, including 27 HiBALs, 10 LoBALs, and 2 FeLoBALs — all of which were found by visual inspection. One object in this supplement (SDSS J235238.08+010552.4) has an intermediate redshift  $z = 2.156$  and two prominent C IV broad absorption troughs. We have included this object in our supplement rather than the main catalog because one trough has a velocity shift too low, and the other too high, for the object to qualify as a BALQSO by the traditional definition. Two of the radio-detected quasars in this supplementary sample are also included in the Menou et al. (2001) analysis. Between Tables 1 and 2 we catalog 224 BALQSOs.

### 4.3. NonBAL Sample

We wish to compare our classes of BALQSOs with a large class of objects with no broad absorption lines. To avoid rediscovering or confusing correlations with luminosity and redshift when comparing nonBALs and BALQSOs, we have created a nonBALQSO sample with essentially identical distributions of absolute magnitudes  $M_{i^*}$  and redshifts in the BALQSO sample.

For each BALQSO (HiBALs and LoBALs), we searched the sample of nonBALQSOs and selected the object with the most similar absolute  $i^*$  magnitude and redshift without



choosing any nonBALQSO more than once. We repeated this process three more times with the remaining nonBALQSOs (without duplication). Each object in the BALQSO sample was thus matched to four nonBALQSOs with similar absolute magnitude and redshift, yielding a nonBALQSO sample with four times as many objects as the BALQSO sample.

Typical deviations in  $M_{i^*}$  and  $z$  between a pair of matched BAL and nonBALQSOs are  $\Delta M_{i^*} \sim 0.06$  mag (slightly higher than 0.03, the systematic photometric error) and  $\Delta z \sim 0.06$ . We performed K-S and Student- $t$  tests (Press et al. 1992) to ensure that the magnitudes and redshifts of the BAL and nonBALQSO samples were consistent.

#### 4.4. BAL and nonBALQSO Composite Spectra

To compare the populations of nonBALQSOs, HiBALs, and LoBALs, we created geometric mean composite spectra for each of these classes of objects. We use the method of Vanden Berk et al. (2001), whereby all spectra from a sample are deredshifted, normalized, binned into wavelength ranges, and geometrically averaged together bin by bin. The HiBAL composite was created from all objects labeled by “Hi” in Column 18 of Tables 1 and 2, the LoBAL composite by those labeled “Lo”, the HiBAL+LoBAL composite by those marked “Hi” or “Lo”, and the FeLoBAL composite by those labeled “FeLo”. The nonBALQSO composite spectrum was created from the matched sample of nonBALQSOs discussed above. These composite spectra are shown in Figure 5. Note that the redness of the BALQSO spectra is not simply the result of the BAL absorption troughs, but rather because the SEDs themselves are redder. If interpreted as extinction, for HiBALs  $E(B - V) \sim 0.023$  and for LoBALs  $E(B - V) \sim 0.077$  (assuming SMC-like dust extinction), but more careful analysis is required to clarify what this means; see Reichard et al. (2003), which will present a comparison of the continuum and emission line features of these composites. In addition, Figure 5 shows that the C IV absorption troughs extend to within  $3000 \text{ km s}^{-1}$  of the peak of the emission line (starting at essentially 0 velocity for the LoBAL composite); see below for further discussion.

## 5. Discussion

### 5.1. BI Comparison

Before we analyze the BI distribution, we first compare our BI values to those from Tolea et al. (2002). In Figure 6 the C IV balnicity indices computed using the fitted composite spectrum (FCS) method from the current paper are plotted against the traditional power

law + Gaussian line (PL+G) results from Tolea et al. (2002). The rms of the differences between the two samples is  $945 \text{ km s}^{-1}$ , but it is not uniform with BI: the rms fractional discrepancy decreases from  $\simeq 1$  for those with  $\text{BI} < 300 \text{ km s}^{-1}$  to  $\simeq 0.25$  for the largest BIs measured ( $> 4,000 \text{ km s}^{-1}$ ). Although the scatter about the line of unit ratio between the two BI measures is nearly symmetric, there is a tendency for the FCS method to give larger BIs to those BALs the PL+G method would assign a value  $< 100 \text{ km s}^{-1}$ .

For single trough HiBALs the scatter in the points from the  $BI_{PL+G} = BI_{FCS}$  line is due mainly to the difference in flux levels from which absorption was measured. BALQSOs with more discrepant BI values can be attributed to a number of causes, most of which are generally related to the placement of the continuum. For all FeLoBALs and some LoBALs, broad absorption can nearly eliminate the object’s continuum in parts of the spectrum. In these cases, fitting a composite spectrum or even a power law to the object is difficult, and there is little chance that the fitted composite spectrum and fitted power law will define similar continua through the C IV broad absorption line. Fortunately, this problem is mitigated to some extent by the fact that any reasonable estimate of the continuum will yield a BI that is appropriately large even if it is not entirely accurate.

In addition, objects with narrower absorption troughs with widths near  $2000 \text{ km s}^{-1}$  (the lower limit on trough widths) may be given a zero balnicity index by one method and a nonzero balnicity index by the other. These quasars might be classified as a nonBALQSO or BALQSO depending on exactly how the flux level before absorption was determined (there are 4 quasars for which the PL+G method finds non-zero BI values and the FCS method finds  $BI = 0$ , and 13 that are the other way around). BALQSOs with multiple or complex troughs also present some problems. Sometimes the continuum placement will be such that one method finds that the entire absorption complex contributes to the BI, whereas another continuum placement will count only part of the absorption complex. Therefore, one also expects that there will be some large discrepancies for objects with relatively large BI values.

Finally, it is important to realize that the redshifts used in the composite method and the redshifts used by Tolea et al. (2002) were derived in slightly different ways. In the mean, the C IV and C III] redshifts differ by  $\simeq 340 \text{ km s}^{-1}$ , but in individual objects the offset of C IV from systemic can be up to  $\sim 2000 \text{ km s}^{-1}$  (Richards et al. 2002b). In the FCS method the redshifts are taken from the EDR quasar catalog (Schneider et al. 2002) and were determined by using the *empirical* wavelengths of the emission lines commonly seen in quasars (Vanden Berk et al. 2001) as opposed to the laboratory wavelengths — thus partially correcting for emission line shifts. On the other hand, the PL+G method directly fit to the emission line profiles of each individual quasar, rather than assuming that all shared the velocity width found in the composite. These different treatments of the emission line

profile are especially important, of course, to BALQSOs with small BIs. It is likely that the relatively large discrepancies found for small BI cases are due to these systematic contrasts.

In conclusion, because the two automated methods disagreed about the *existence* of a BAL feature in only very few cases, we believe that they have mutually validated each other as methods for deciding whether broad absorption is present in quasar spectra. In addition, when the feature is strong, the two methods agree reasonably well with regard to its magnitude (the BI measure). However, for weaker features, there can be significant discrepancies between the BIs produced by the two methods; we must therefore acknowledge a significant systematic uncertainty in the smaller BI range. It is exactly for these cases that the arbitrariness in the parameters of the classical BI definition (e.g., the minimum offset, the minimum width of continuous absorption) creates at least as great a systematic uncertainty in determining the *physical* “balnicity” (Hall et al. 2002).

## 5.2. Balnicity Index Distribution

The distribution of balnicity indices using the FCS (solid histogram) and PL+G (as measured by Tolea et al. 2002, dashed histogram) methods to define continua are shown in Figure 7. The two distributions are very similar; each shows a large fraction of BALQSOs with small balnicity indices and a shallow tail of BALQSOs with large balnicities. The BI distribution goes roughly as  $BI^{-1}$ , where the  $-1$  power-law index (gray line in Fig. 7) is *not* a fit to the data, but rather is meant to guide the eye. The inset to Figure 7 shows that both the distribution appears to change significantly for moderate BI ( $\lesssim 1500 \text{ km s}^{-1}$ ) and that the PL+G method yields more objects with BI  $\lesssim 100 \text{ km s}^{-1}$ ; see below for more details.

Comparison of these distributions with that from the Weymann et al. (1991) sample show significant differences. Weymann et al. (1991) computed C IV balnicity indices for 42 BALs. Two BALs (5%) were “borderline” cases, with C IV balnicity indices  $< 600 \text{ km s}^{-1}$ , 18 BALs (43%) had balnicity indices  $> 5000 \text{ km s}^{-1}$ , and three BALs (7%) had balnicity indices  $> 10,000 \text{ km s}^{-1}$ . In our sample, we find that C IV balnicity indices are generally smaller. Only two objects (1%) out of the 185 in our complete BAL sample (Table 1) possessed a C IV balnicity index above  $10,000 \text{ km s}^{-1}$  (these were further classified by eye as LoBALs), and only 14 (8%) have a balnicity index above  $5000 \text{ km s}^{-1}$ . The differences between the balnicity index distribution of Weymann et al. (1991) and ours could be the result of the differences in continuum and emission line fitting methods, small number statistics, or our sample being more complete to quasars with lower BI values.

The C IV balnicity indices of our LoBAL sample of 24 objects (from Table 1) were

also generally less than those of the entire BALQSO sample of Weymann et al. (1991). Our LoBAL sample has 6 objects (25%) with C IV balnicity indices  $> 5000 \text{ km s}^{-1}$ , 2 of the latter having C IV balnicity indices over  $10000 \text{ km s}^{-1}$ . We find that the median LoBAL C IV balnicity index is  $3544 \text{ km s}^{-1}$  as computed using the fitted composite spectrum continuum and  $3468 \text{ km s}^{-1}$  using the power law + Gaussian line continuum; the HiBAL medians are  $937 \text{ km s}^{-1}$  and  $567 \text{ km s}^{-1}$ , respectively. LoBALs exhibit much deeper C IV broad absorption troughs than HiBAL/nonLoBALs, as noted by Weymann et al. (1991), which is normally interpreted as evidence that HiBALs and LoBALs are not distinct types, but rather represent the extremes of a continuum in absorption strength/ionization.

The fact that much of our sample has rather small BI strongly suggests a connection between BAL troughs and the so-called “associated absorbers” (Foltz et al. 1986) that occur within  $\sim 3000 \text{ km s}^{-1}$  of the emission redshift of some quasars (particularly steep-spectrum radio-loud quasars). However, we stress that the details of the shape of the BI distribution for  $BI \ll 1000 \text{ km s}^{-1}$  are not well-determined. Part of the uncertainty is the relatively large systematic error discussed in § 5.1. A larger problem lurks in the arbitrariness of the BI definition. If the minimum width of continuous absorption were fixed at, say,  $1500 \text{ km s}^{-1}$ , numerous additional quasars with weaker absorption (or choppy absorption profiles) would be classified as BALQSOs. In fact, the large number of small BI BALQSOs means that, in this work and all previous work that imposed the Weymann et al. (1991) balnicity criteria, the fraction of quasars with intrinsic outflows has been *significantly* underestimated since those quasars that just barely fail to satisfy the BAL criteria would populate the small BI end of the distribution where the density of objects per BI is greatest.

Furthermore, the LoBAL composite spectrum and both HiBAL composite spectra show significant broad absorption within  $3000 \text{ km s}^{-1}$  of the C IV emission line peak. Thus, the balnicity index definition given by Weymann et al. (1991) needs adjustment if we are to define an index that includes *all* BAL-like outflowing absorption, including that in SDSS J235238.08+010552.4 of Table 2 (which has very high velocity absorption as opposed to very low velocity absorption). Suggestions for alternative balnicity indices were proposed by Hall et al. (2002) and will be considered in more detail in future work on SDSS BALQSOs.

## 6. Conclusions

We have presented a catalog of 224 BALQSOs from the SDSS Early Data Release Quasar Catalog. This sample represents a significant increase in the total number of cataloged BALQSOs. Of these 224 BALQSOs, 185 occupy a region in redshift space where our catalog should be relatively complete to most BALQSOs. Imposing further constraints upon the

initial selection of these objects as quasar candidates leaves us with a relatively homogeneous catalog with 131 BALQSOs.

A comparison of the catalog that results from using our fitted composite spectrum continuum method of classifying quasars as BALQSOs to the BALQSOs sample constructed by Tolea et al. (2002) using the more traditional power-law plus Gaussian continuum method demonstrates that the two methods agree reasonably well when the absorption is relatively strong. Given this agreement, extending our method to make use of multiple templates should allow for even better and more sensitive BALQSO classification in the future.

In agreement with Tolea et al. (2002), we find that the distribution of balnicity indices rises rapidly with decreasing balnicity index. Our C IV balnicity indices tend to be less than  $5000 \text{ km s}^{-1}$  and hence less than those given by Weymann et al. (1991). Furthermore, even though we ignored absorption within  $3000 \text{ km s}^{-1}$  of the adopted redshift when defining our BALQSO sample, C IV broad absorption troughs extend within  $3000 \text{ km s}^{-1}$  of the expected emission center for BALs, and the absorption in LoBALs can start at velocities as low as  $0 \text{ km s}^{-1}$  from the expected emission center. The combination of these results strongly suggests that the Weymann et al. (1991) BALQSO definition is too strict in terms of identifying quasars with intrinsic outflows and that the true fraction of quasars with such outflows may be significantly larger than estimated in the past (or herein). If there are numerous quasars with comparatively weak “broad” absorption, it will, of course, be very difficult to separate them from those with genuine “associated absorbers”. It is possible that the associated absorber ( $z_{em} \simeq z_{abs}$ ) population is merely the weak tail of the BALQSO distribution (and that FeLoBALs and LoBALs are simply the strong tail of the same distribution).

Funding for the creation and distribution of the SDSS Archive has been provided by the Alfred P. Sloan Foundation, the Participating Institutions, the National Aeronautics and Space Administration, the National Science Foundation, the U.S. Department of Energy, the Japanese Monbukagakusho, and the Max Planck Society. The SDSS Web site is <http://www.sdss.org/>. The SDSS is managed by the Astrophysical Research Consortium (ARC) for the Participating Institutions. The Participating Institutions are The University of Chicago, Fermilab, the Institute for Advanced Study, the Japan Participation Group, The Johns Hopkins University, Los Alamos National Laboratory, the Max-Planck-Institute for Astronomy (MPIA), the Max-Planck-Institute for Astrophysics (MPA), New Mexico State University, University of Pittsburgh, Princeton University, the United States Naval Observatory, and the University of Washington. T. A. R., G. T. R., and D. P. S. were supported by National Science Foundation grant AST99-00703. P. B. H. is supported by FONDECYT grant 1010981. We thank Niel Brandt for reading an early draft of the manuscript.

## REFERENCES

- Baldwin, J. A. 1977, *ApJ*, 214, 679
- Becker, R. H., White, R. L., Gregg, M. D., Brotherton, M. S., Laurent-Muehleisen, S. A., & Arav, N. 2000, *ApJ*, 538, 72
- Becker, R. H., White, R. L., & Helfand, D. J. 1995, *ApJ*, 450, 559
- Blanton et al. 2002, *AJ*, submitted
- Boroson, T. A. & Meyers, K. A. 1992, *ApJ*, 397, 442
- Brotherton, M. S., Tran, H. D., Becker, R. H., Gregg, M. D., Laurent-Muehleisen, S. A., & White, R. L. 2001, *ApJ*, 546, 775
- Cardelli, J. A., Clayton, G. C., & Mathis, J. S. 1989, *ApJ*, 345, 245
- Foltz, C. B., Weymann, R. J., Peterson, B. M., Sun, L., Malkan, M. A., & Chaffee, F. H. 1986, *ApJ*, 307, 504
- Fukugita, M., Ichikawa, T., Gunn, J. E., Doi, M., Shimasaku, K., & Schneider, D. P. 1996, *AJ*, 111, 1748
- Gunn, J. E., Carr, M., Rockosi, C., Sekiguchi, M., Berry, K., Elms, B., de Haas, E., Ivezić, Ž., et al. 1998, *AJ*, 116, 3040
- Hall, P. B., Anderson, S. F., Strauss, M. A., York, D. G., Richards, G. T., Fan, X., Knapp, G. R., Schneider, D. P., et al. 2002, *ApJS*, 141, 267
- Hewett, P. C., Foltz, C. B., & Chaffee, F. H. 1995, *AJ*, 109, 1498
- Hogg, D. W., Finkbeiner, D. P., Schlegel, D. J., & Gunn, J. E. 2001, *AJ*, 122, 2129
- Menou, K., Vanden Berk, D. E., Ivezić, Ž., Kim, R. S. J., Knapp, G. R., Richards, G. T., Strateva, I., Fan, X., et al. 2001, *ApJ*, 561, 645
- Mihalas, D. & Binney, J. 1981, *Galactic Astronomy: Structure and Kinematics* (San Francisco, CA, W. H. Freeman and Co.)
- Nandy, K., Morgan, D. H., Willis, A. J., Wilson, R., & Gondhalekar, P. M. 1981, *MNRAS*, 196, 955
- Ogle, P. M., Cohen, M. H., Miller, J. S., Tran, H. D., Goodrich, R. W., & Martel, A. R. 1999, *ApJS*, 125, 1

- Osmer, P. S., Porter, A. C., & Green, R. F. 1994, *ApJ*, 436, 678
- Pei, Y. C. 1992, *ApJ*, 395, 130
- Pier et al. 2002, *AJ*, submitted
- Press, W. H., Teukolsky, S. A., Vetterling, W. T., & Flannery, B. P. 1992, *Numerical recipes in C. The art of scientific computing* (Cambridge: University Press, —c1992, 2nd ed.)
- Prevot, M. L., Lequeux, J., Prevot, L., Maurice, E., & Rocca-Volmerange, B. 1984, *A&A*, 132, 389
- Reichard et al. 2003, *AJ*, in preparation
- Richards, G. T., Fan, X., Newberg, H. J., Strauss, M. A., Vanden Berk, D. E., Schneider, D. P., Yanny, B., Boucher, A., et al. 2002a, *AJ*, 123, 2945
- Richards, G. T., Fan, X., Schneider, D. P., Vanden Berk, D. E., Strauss, M. A., York, D. G., Anderson, J. E., Tremonti, C., et al. 2001, *AJ*, 121, 2308
- Richards, G. T., Vanden Berk, D. E., Reichard, T. A., Hall, P. B., Schneider, D. P., SubbaRao, M., Thakar, A. R., & York, D. G. 2002b, *AJ*, 124, 1
- Richards et al. 2003, *AJ*, submitted
- Savage, B. D. & Mathis, J. S. 1979, *ARA&A*, 17, 73
- Schlegel, D. J., Finkbeiner, D. P., & Davis, M. 1998, *ApJ*, 500, 525
- Schmidt, G. D. & Hines, D. C. 1999, *ApJ*, 512, 125
- Schneider, D. P., Richards, G. T., Fan, X., Hall, P. B., Strauss, M. A., Vanden Berk, D. E., Gunn, J. E., Newberg, H. J., et al. 2002, *AJ*, 123, 567
- Smith, J. A., Tucker, D. L., Kent, S., Richmond, M. W., Fukugita, M., Ichikawa, T., Ichikawa, S., Jorgensen, A. M., et al. 2002, *AJ*, 123, 2121
- Sprayberry, D. & Foltz, C. B. 1992, *ApJ*, 390, 39
- Stoughton, C., Lupton, R. H., Bernardi, M., Blanton, M. R., Burles, S., Castander, F. J., Connolly, A. J., Eisenstein, D. J., et al. 2002, *AJ*, 123, 485
- Surdej, J. & Hutsemekers, D. 1987, *A&A*, 177, 42
- Tolea, A., Krolik, J. H., & Tsvetanov, Z. 2002, *ApJ*, 578, L31

- Turnshek, D. A. 1984, ApJ, 280, 51
- Vanden Berk, D. E., Richards, G. T., Bauer, A., Strauss, M. A., Schneider, D. P., Heckman, T. M., York, D. G., Hall, P. B., et al. 2001, AJ, 122, 549
- Voges, W., Aschenbach, B., Boller, T., Bräuninger, H., Briel, U., Burkert, W., Dennerl, K., Englhauser, J., et al. 1999, A&A, 349, 389
- Voit, G. M., Weymann, R. J., & Korista, K. T. 1993, ApJ, 413, 95
- Weymann, R. J. 1995, in QSO Absorption Lines, Proceedings of the ESO Workshop Held at Garching, Germany, 21 - 24 November 1994, edited by Georges Meylan. Springer-Verlag Berlin Heidelberg New York. Also ESO Astrophysics Symposia, 1995., p.213, 213
- Weymann, R. J., Morris, S. L., Foltz, C. B., & Hewett, P. C. 1991, ApJ, 373, 23
- White, R. L., Becker, R. H., Gregg, M. D., Laurent-Muehleisen, S. A., Brotherton, M. S., Impey, C. D., Petry, C. E., Foltz, C. B., et al. 2000, ApJS, 126, 133
- Wilkes, B. J. 1986, MNRAS, 218, 331
- Yamamoto, T. M. & Vansevičius, V. 1999, PASJ, 51, 405
- York, D. G., Adelman, J., Anderson, J. E., Anderson, S. F., Annis, J., Bahcall, N. A., Bakken, J. A., Barkhouser, R., et al. 2000, AJ, 120, 1579



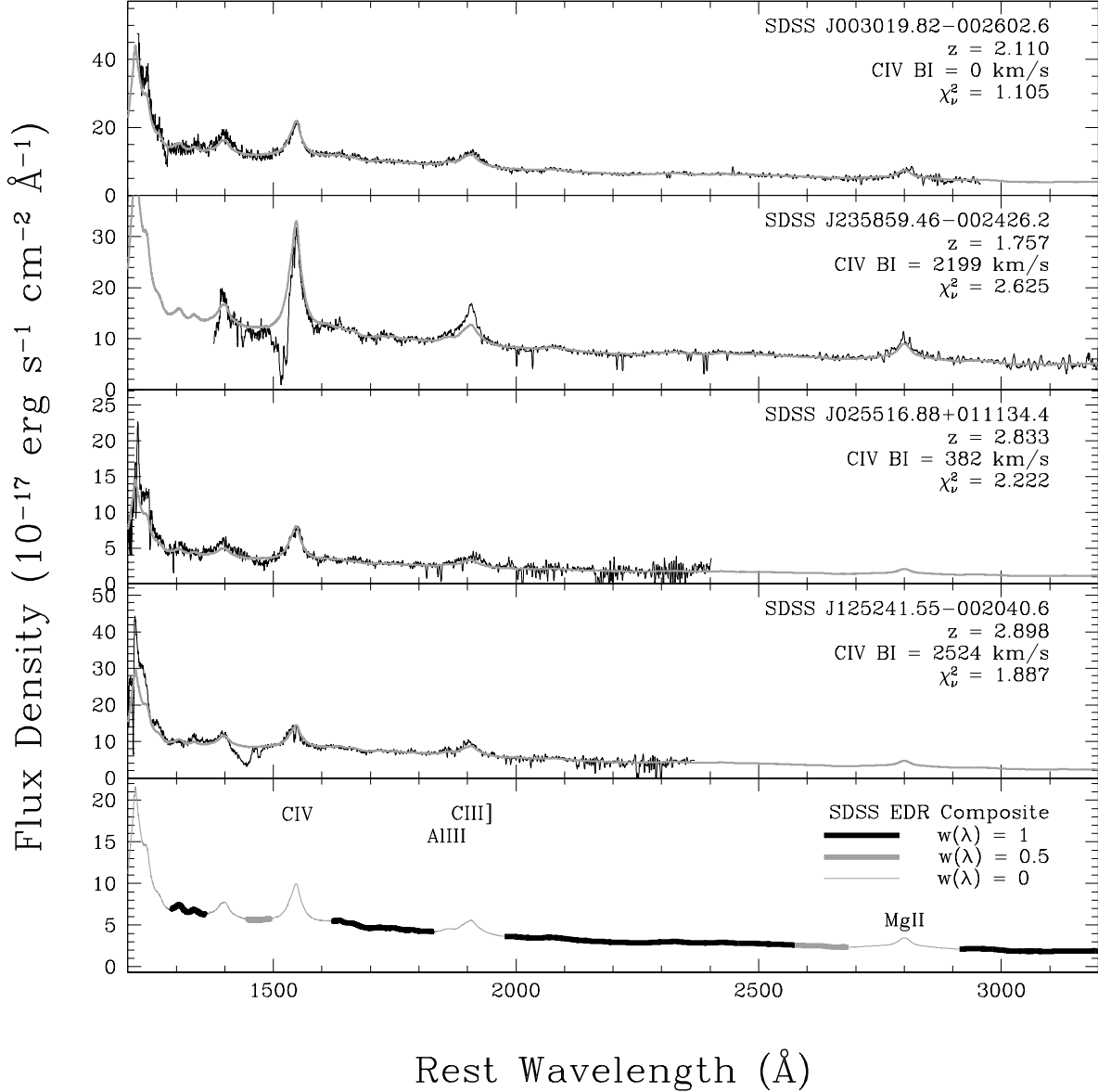


Fig. 1.— EDR composite spectrum fits (*gray*) for four quasar spectra (*black*) from the EDR sample: one nonBAL (*top panel*) and three HiBALs (*middle three panels*). Note how well the composite fitting method can recover BALQSOs with very weak absorption troughs such as the BALQSO shown in the third panel. The EDR composite spectrum is fitted by a power law with SMC reddening. The C IV emission line of the EDR composite has been scaled to match the peak line flux of each object. The spectra are normalized at  $1725(1+z)$  Å. The last panel shows the weights as a function of wavelength that were used during our composite fitting procedure; see text for more details.

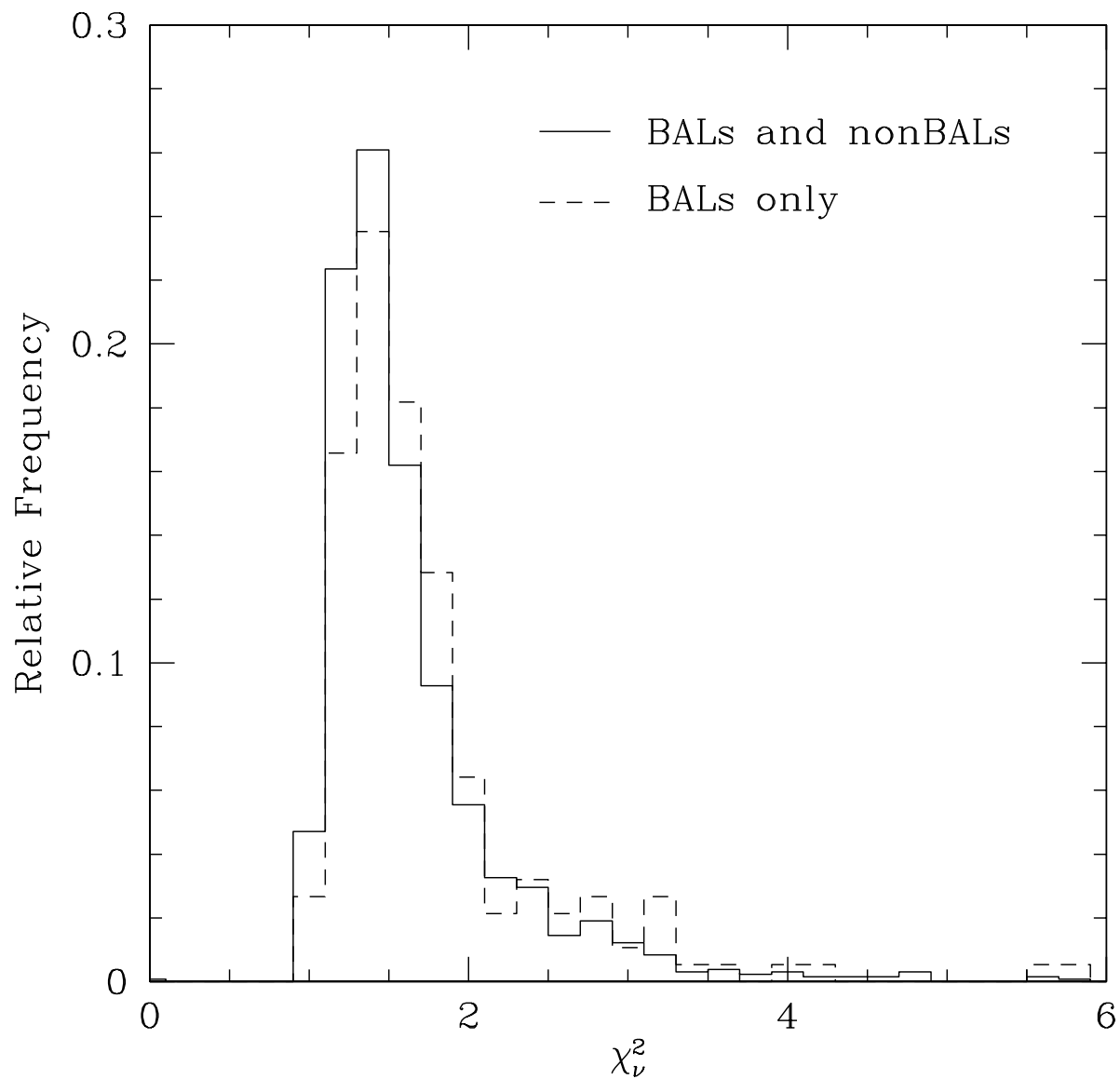


Fig. 2.— Distribution of  $\chi^2_\nu$  values for all the objects in the redshift range searched for BAL troughs (*solid line*) and for all quasars that we have classified as BALQSOs (*dashed line*). Quasars with  $\chi^2_\nu \lesssim 2.5$  are considered to have good fits. Larger values indicate either bad fits, or significant absorption.

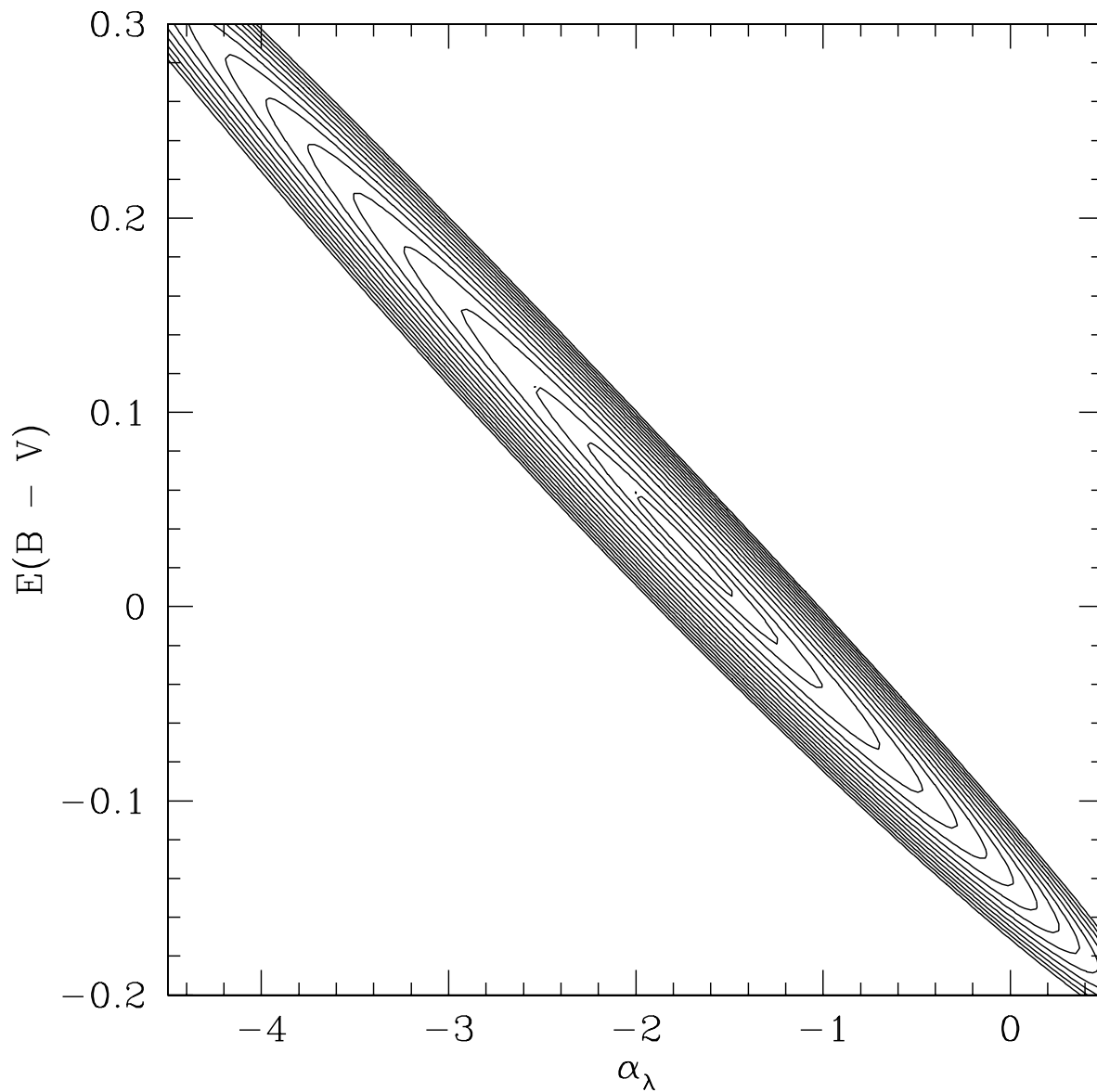


Fig. 3.— A contour plot of a the reduced  $\chi^2$  values that result from fitting a composite spectrum continuum onto an individual spectrum (SDSS J003019.82–002802.6,  $\chi_\nu^2 = 1.105$ , top panel of Fig. 1) by changing the spectral index and reddening according to the SMC reddening law. The contour levels range from  $\chi_\nu^2 = 1.12$  (center curve) to  $\chi_\nu^2 = 2.5$  (outer curve).

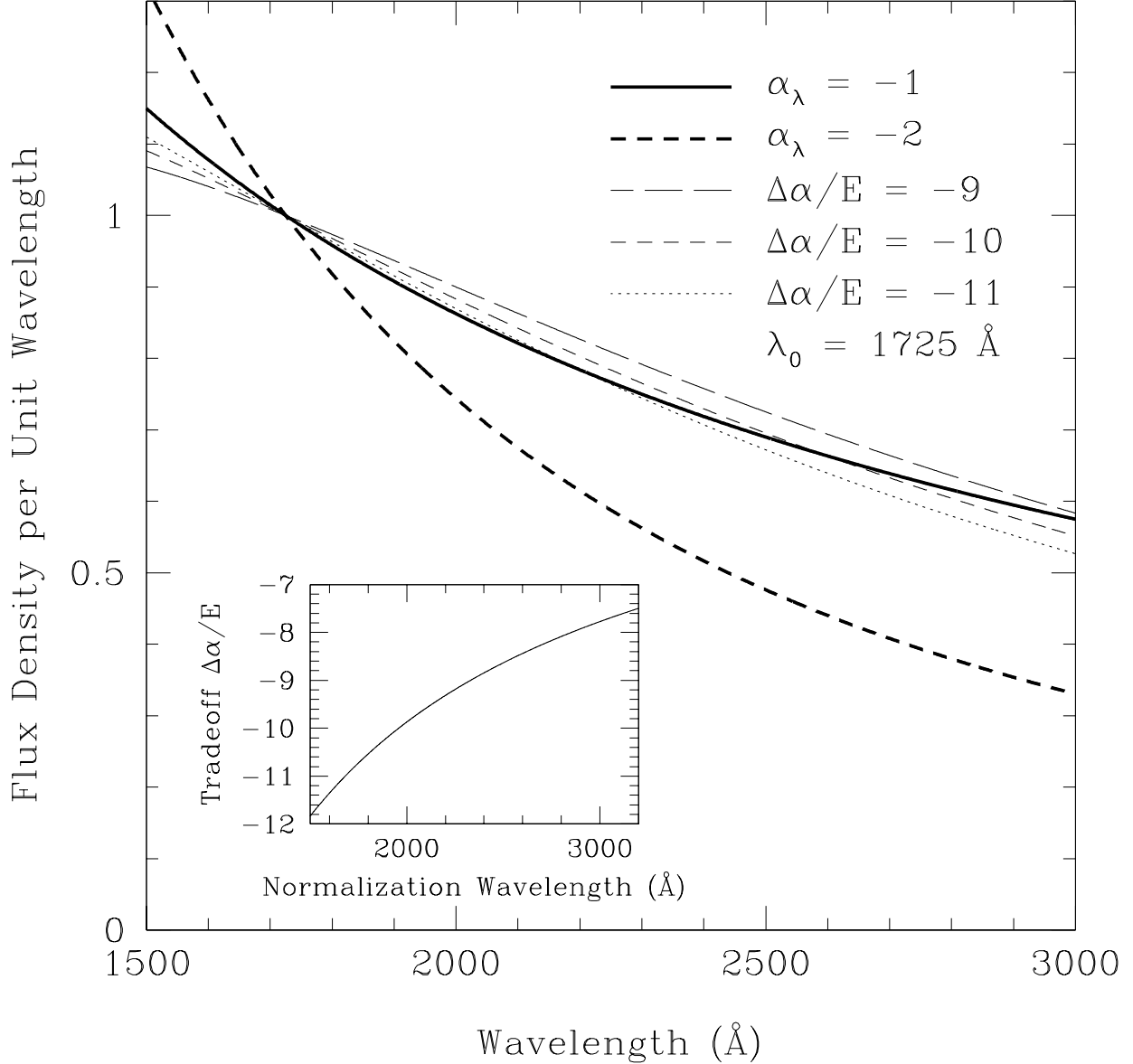


Fig. 4.— The degeneracy of spectral index and reddening allows a blue power law ( $\alpha = -2$ , *thick dashed line*) to approximate a red power law ( $\alpha = -1$ , *thick solid line*) by reddening according to an SMC-like reddening law. The blue power law is reddened with three amounts of reddening:  $E(B - V) = 0.111$  (*thin long-dashed line*),  $0.100$  (*thin short-dashed line*), and  $0.091$  (*thin dotted line*), corresponding to  $\beta = \Delta\alpha/E = -9, -10,$  and  $-11$ . (*Inset*) The mean tradeoff  $\beta = \Delta\alpha/E$  between spectral index and reddening for the wavelength range  $1500 \text{ \AA} < \lambda < 3200 \text{ \AA}$ . A change in spectral index can be compensated by a change in reddening multiplied by the tradeoff factor, which depends on the normalization wavelength.

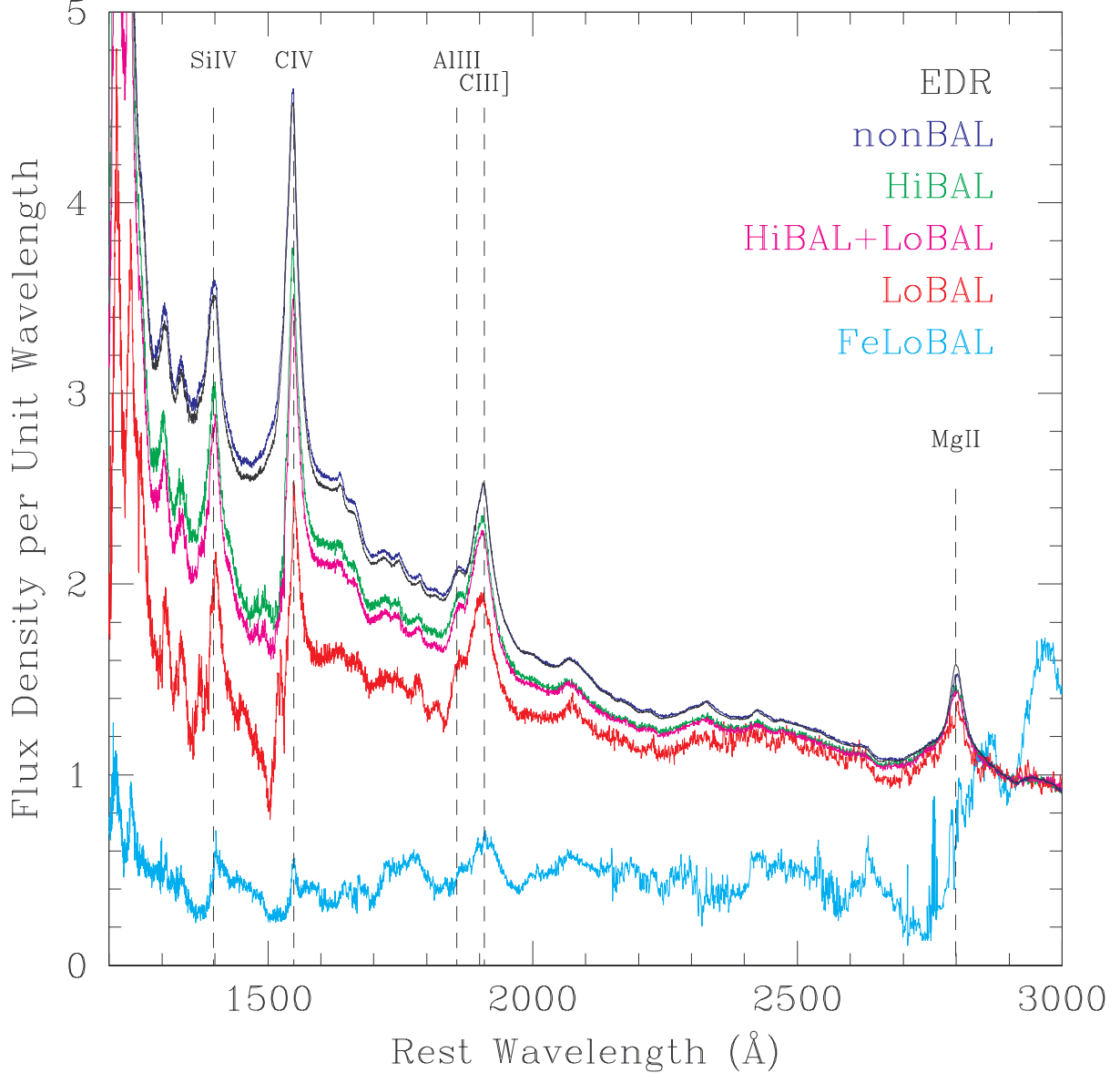


Fig. 5.— The normalized composite spectra of the full EDR quasar sample (*black*), non-BALs (*blue*), HiBALs (including LoBALs, *magenta*), HiBAL/nonLoBALs (excluding LoBALs, *green*), LoBALs (*red*), and FeLoBALs (*cyan*). The spectra are similar at long wavelengths above 2400 Å (with the exception of the FeLoBAL composite — which also shows emission near 2950 Å), but the BALQSO composite spectra show clear flux deficits at shorter wavelengths as compared to the nonBALQSO composite spectrum; see Hall et al. (2002) for further details with regard to the absorption structures seen in FeLoBALs. Note that the redness of the BALQSO spectra is not simply the result of the BAL absorption troughs, but rather because the SEDs themselves are redder.

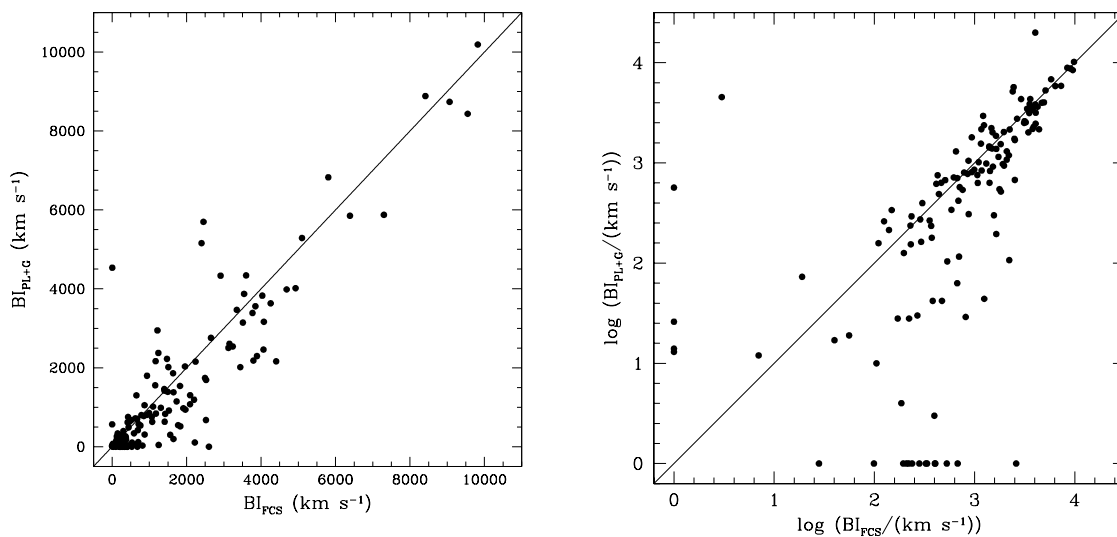


Fig. 6.— Comparison of the C IV balnicity indices computed by using a fitted composite spectrum ( $BI_{FCS}$ ) and by using a power law + Gaussian line ( $BI_{PL+G}$ ). The left-hand panel shows the balnicity indices in a linear representation; the right-hand panel shows the same data in a log-log representation, which emphasizes the small BI end of the distribution. Quasars that were found to have  $BI = 0$  by either method but that we believe to be true BALQSOs are plotted with  $\log(BI) = 0$  on the appropriate axis.

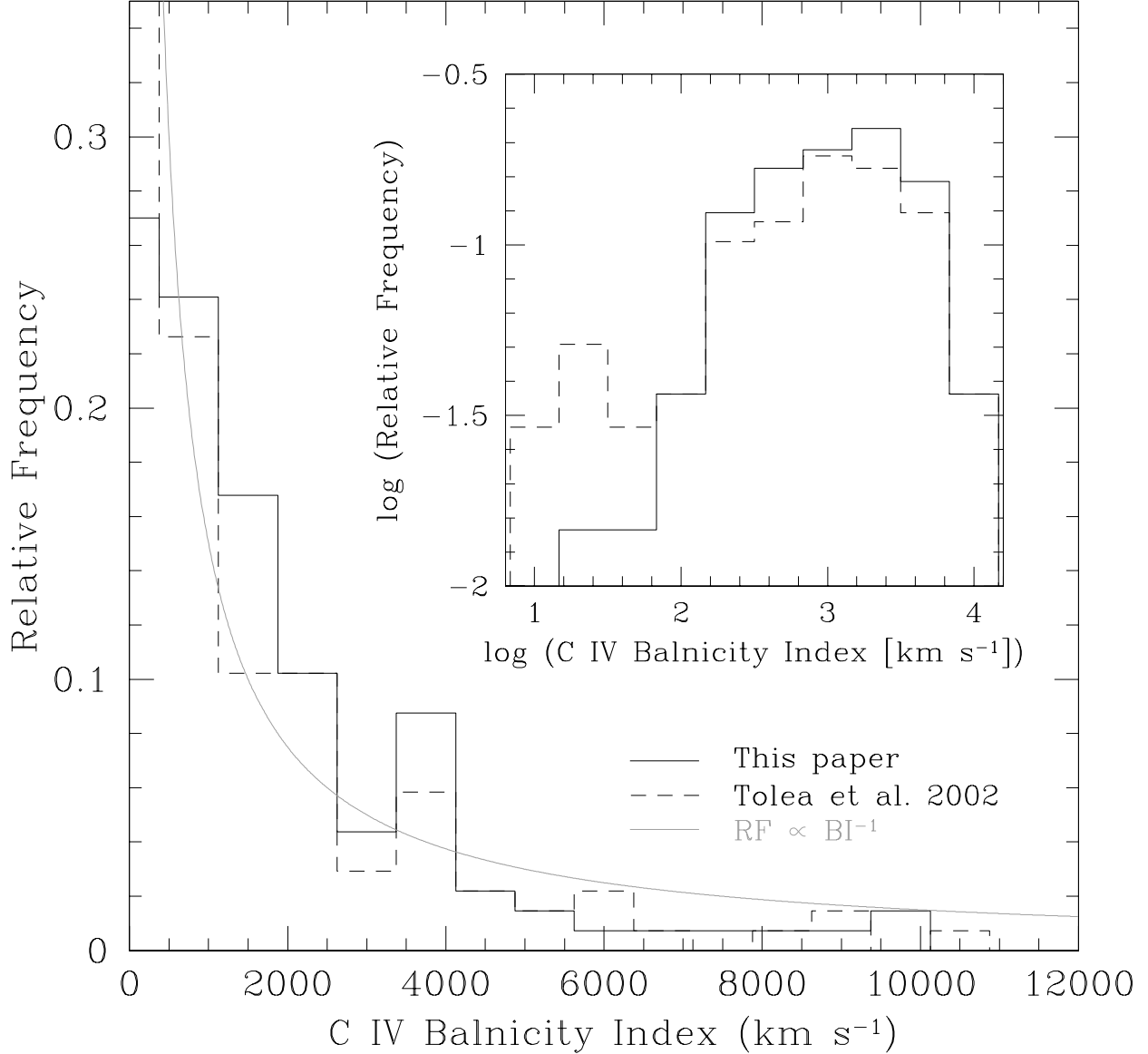


Fig. 7.— The C IV balnicity index distribution of BALQSOs. These histograms show the distribution of the balnicity indices as computed with the fitted EDR composite spectrum (*solid histogram*) and using a power law + Gaussian line (*dashed histogram*, Tolea et al. 2002). The solid gray line depicts a distribution that is proportional to  $\text{BI}^{-1}$ ; it is not a fit to the data, but rather it is merely meant to guide the eye. The inset is a log-log version of the plot; it emphasizes the smaller end of the BI distribution and shows an apparent change in BI distribution towards smaller BI ( $\lesssim 1500 \text{ km s}^{-1}$ ; not to be confused with the differences between the two methods for  $\text{BI} \lesssim 100 \text{ km s}^{-1}$ ).

Table 1. SDSS EDR BALQSO Catalog — Objects with  $1.7 \leq z \leq 4.2$ 

SDSS Object (1)	Plate (2)	Fiber (3)	MJD (4)	Target <sup>a</sup>			$f_{20\text{cm}}$ (mJy) (8)	Redshift (9)	$i^*$ (10)	Dereddened $M_{i^*}$ (11)	C IV $BI^b$ (12)	C IV $BI^c$ (13)	Mg II $BI^b$ (14)	Classification <sup>d</sup>			Sub- sample (18)
				F (5)	E (6)	S (7)								1 (15)	2 (16)	3 (17)	
000056.89–010409.8	387	98	51791	1	1	0	0.00	2.111	19.09	−26.34	1560	300	...	H	H	Hi	Hi
001025.90+005447.6	389	332	51795	1	1	1	0.00	2.845	18.78	−27.26	4405	2163	...	H	H	Hiz	Hi
001438.28–010750.2	389	211	51795	1	1	1	1.41	1.813	18.33	−26.78	0	13	...	N	H	Hi	Hi
001502.26+001212.4	389	465	51795	1	1	1	0.00	2.857	18.87	−27.17	938	809	...	H	H	Hiz	Hi
001824.96+001525.8	390	394	51900	0	1	0	0.00	2.430	19.55	−26.16	3347	3468	...	H	H	Loz	Lo
002127.88+010420.2	390	443	51900	1	1	1	0.00	1.829	18.01	−27.12	40	17	...	H	H	Hi	Hi
003551.98+005726.3	392	449	51793	1	1	0	0.00	1.905	18.76	−26.46	1731	1148	...	H	H	Hi	Hi
004041.39–005537.3	393	298	51794	1	1	0	0.00	2.092	17.91	−27.50	0	14	...	N	H	no	Hi
004118.58+001742.5	392	631	51793	1	1	1	0.00	1.764	18.41	−26.64	1384	...	...	H	...	Hi	Hi
004323.43–001552.5	393	181	51794	0	1	0	0.00	2.806	17.96	−28.05	588	340	...	H	H	Hiz	Hi
004613.53+010425.7	393	572	51794	1	1	0	3.04	2.152	17.73	−27.73	3151	2608	...	H	H	Hi	Hi
004732.72+002111.4	393	588	51794	1	1	0	0.00	2.879	18.60	−27.47	369	235	...	H	H	Hiz	Hi
005001.81+002620.0	394	425	51876	1	1	0	0.00	1.936	18.93	−26.32	0	26	...	N	H	no	Hi
005355.15–000309.3	395	352	51783	1	1	1	0.00	1.715	17.93	−27.07	1088	...	...	H	...	Hi	Hi
005419.99+002727.9	394	514	51876	0	1	0	0.00	2.522	18.13	−27.66	786	802	...	H	H	Hiz	Hi
005703.39+001408.1	395	394	51783	1	1	0	0.00	3.036	19.43	−26.74	3124	2504	...	H	H	Hiz	Hi
005830.16+005130.0	395	446	51783	1	1	0	0.00	1.833	18.97	−26.16	19	73	...	H	H	Hi?	Hi
005837.30–003553.7	395	148	51783	1	1	1	0.00	1.810	18.97	−26.14	4075	3166	...	H	H	Hi	Hi
010241.04–004208.8	396	261	51816	1	1	1	0.00	1.742	18.74	−26.29	0 <sup>e</sup>	...	...	N	...	Hi	Hi
010336.40–005508.7	396	297	51816	0	1	0	0.00	2.442	19.68	−26.05	99	0	...	H	N	Hiz	Hi
010612.21+001920.1	396	553	51816	1	1	0	0.00	3.110	18.16	−28.06	2453	5698	...	H	H	Hi	Hi
010616.05+001523.9	396	552	51816	0	1	0	0.00	3.050	19.73	−26.45	2520	676	...	H	H	Hiz	Hi
011227.60–011221.7	397	122	51794	1	1	0	0.00	1.755	17.57	−27.47	3033	...	...	H	...	Hi	Hi
011237.35+001929.7	397	513	51794	1	1	0	0.00	2.695	19.53	−26.40	760	538	...	H	H	Hi?	Hi
011251.12+000921.2	397	510	51794	0	1	1	0.00	2.865	19.64	−26.42	6388	5852	...	H	H	Hiz	Hi
011948.51+004356.0	398	531	51789	1	1	1	0.00	1.772	17.99	−27.07	1	...	...	H	...	Hi	Hi
012913.70+011428.0	399	604	51817	1	1	0	0.00	1.782	18.59	−26.48	345	...	...	H	...	Hi	Hi
013233.89+011607.1	400	414	51820	1	1	1	0.00	1.786	18.66	−26.42	514	...	...	H	...	Hi	Hi
013656.31–004623.9	400	3	51820	1	1	1	0.00	1.709	17.83	−27.16	1304	...	...	H	...	Hi	Hi
014515.58+002931.0	401	595	51788	1	1	0	0.00	3.006	19.80	−26.35	8413	8885	...	H	H	Loz	Lo
014705.43–004148.9	402	271	51793	0	1	0	0.00	2.108	19.01	−26.41	4926	4017	...	H	H	Lo	Lo
014812.80–005108.8	402	299	51793	1	1	1	3.19	1.816	18.30	−26.82	1217	2947	...	H	H	Hi	Hi
014836.33+000511.5	402	429	51793	1	1	0	0.00	3.339	19.66	−26.70	4065	2461	...	H	H	hiz	Hi
014905.27–011404.9 <sup>f</sup>	402	246	51793	1	1	0	0.00	1.960	19.51	−25.76	...	...	...	...	N	Fe?Lo	FeLo
015024.44+004432.9	402	485	51793	1	1	0	0.00	1.990	18.86	−26.44	937	1798	...	H	H	Hi	Hi
015048.82+004126.2	402	505	51793	1	1	0	0.00	3.703	18.26	−28.31	105	10	...	H	H	Hiz	Hi
020006.31–003709.7	403	70	51871	0	1	0	0.00	2.136	18.19	−27.26	9550	8435	...	H	H	Lo	Lo
020529.19–000912.9	404	165	51812	0	1	0	0.00	2.350	19.94	−25.71	3	4535	...	H	H	Loz	Lo
021327.25–001446.9	405	197	51816	0	1	0	0.00	2.399	19.96	−25.73	700	116	...	H	H	Hiz	Hi
021606.40+011509.5	405	570	51816	1	1	0	0.00	2.223	18.47	−27.06	2495	1740	...	H	H	Hi	Hi
022505.06+001733.2	406	507	51817	0	1	0	0.00	2.422	19.28	−26.43	1099	1016	...	H	H	Loz	Lo
022716.73–001317.1	406	71	51817	0	0	1	0.00	1.980	19.73	−25.56	561	...	...	H	...	Hi	Hi
022844.09+000217.0	406	35	51817	1	1	0	0.00	2.716	17.68	−28.26	1823	1539	...	H	H	HizLo?	Lo
023139.52+001758.4	407	483	51820	1	1	1	0.00	2.360	18.81	−26.85	125	261	...	H	H	Hiz	Hi
023153.78–003232.1	407	163	51820	1	1	0	0.00	1.721	18.63	−26.37	108	...	...	H	...	Hi?	Hi
023252.80–001351.2	407	158	51820	1	1	1	0.00	2.025	18.62	−26.72	2092	1076	...	H	H	Hi	Hi
023600.49+011113.3	408	324	51821	0	0	1	0.00	1.826	19.73	−25.40	28	0	...	H	N	Hi	Hi
023908.98–002121.4	408	179	51821	1	1	0	0.00	3.777	19.49	−27.12	2655	2758	...	H	H	Hiz	Hi



Table 1—Continued

SDSS Object (1)	Plate (2)	Fiber (3)	MJD (4)	Target <sup>a</sup>			$f_{20\text{cm}}$ (mJy) (8)	Redshift (9)	$i^*$ (10)	Dereddened $M_{i^*}$ (11)	C IV $BI^b$ (12)	C IV $BI^c$ (13)	Mg II $BI^b$ (14)	Classification <sup>d</sup>			Sub- sample (18)
				F (5)	E (6)	S (7)								1 (15)	2 (16)	3 (17)	
024221.86+004912.7	408	576	51821	1	1	1	0.00	2.071	18.03	-27.36	229	237	...	H	H	Hi	Hi
024304.68+000005.4	408	80	51821	1	1	1	0.00	2.003	17.98	-27.34	301	397	...	H	H	Hi	Hi
024457.18-010809.9	409	282	51871	1	1	0	0.00	3.960	18.31	-28.40	3630	...	...	H	...	HiZ	Hi
025042.45+003536.7	410	352	51816	0	1	0	0.00	2.380	18.31	-27.37	3544	3873	...	H	H	Loz	Lo
025204.28+003137.0	410	383	51816	1	1	1	0.00	4.100	19.46	-27.32	259	...	...	H	...	HiZ	Hi
025247.34+005135.1	409	612	51871	1	1	0	0.00	2.112	18.74	-26.68	441	489	...	H	H	no	Hi
025331.93+001624.7	410	391	51816	1	1	0	0.00	1.825	18.55	-26.58	186	4	...	H	H	Hi	Hi
025516.88+011134.4	410	450	51816	0 <sup>h</sup>	0	0	0.00	2.833	18.81	-27.22	382	42	...	H	H	no	Hi
025747.75-000503.0	410	117	51816	0	0	1	0.00	2.192	19.79	-25.72	2239	2156	...	H	H	Hi	Hi
030437.22+004729.1	411	504	51817	0	1	0	0.00	2.425	18.88	-26.83	1648	1380	...	H	H	HiZ	Hi
031227.13-003446.2	412	108	51931	1	1	1	0.00	1.772	18.85	-26.21	0 <sup>e</sup>	...	...	N	...	Hi	Hi
031609.83+004043.0	413	387	51929	0 <sup>h</sup>	0	0	0.00	2.902	18.33	-27.75	140	214	...	H	H	HiZ	Hi
031828.90-001523.2	413	170	51929	1	1	0	0.00	1.990	17.85	-27.45	231	154	...	H	H	Hi	Hi
032118.21-010539.9	413	48	51929	0	1	0	...	2.412	17.45	-28.25	...	537	...	...	H	Fe?Loz	FeLo
032125.79+001359.3	413	551	51929	1	1	1	...	1.704	18.89	-26.09	1587	...	...	H	...	Hi?	Hi
032701.43-002207.2	414	152	51869	0	1	0	...	2.325	18.58	-27.05	710	573	...	H	H	HiZ	Hi
033048.51-002819.6	415	268	51810	0	1	0	...	1.779	18.79	-26.28	5548	...	...	H	...	Hi	Hi
033335.03-004927.0	415	138	51810	1	1	1	...	1.776	18.61	-26.46	299	...	...	H	...	no	Hi
094745.27-004113.2	266	5	51630	1	1	0	4.67	2.835	18.85	-27.18	690	419	...	H	H	HiZ	Hi
095048.48-000017.7	267	224	51608	0	1	0	0.00	1.876	19.46	-25.72	194	0	660	H	N	Lo	Lo
100809.63-000209.9	269	31	51910	0	1	0	0.00	2.561	19.35	-26.48	56	19	...	H	H	no	Hi
102258.15-004052.1	272	219	51941	1	1	0	0.00	1.758	18.26	-26.79	998	...	...	H	...	no	Hi
102517.58+003422.0	272	501	51941	1	1	0	0.00	1.888	18.06	-27.13	993	856	...	H	H	Hi	Hi
102527.43-000519.1	272	156	51941	0	1	1	0.00	1.897	18.52	-26.69	149	338	...	H	H	Hi	Hi
103544.96-002924.8	273	69	51957	1	1	0	0.00	2.070	18.64	-26.75	0	567	...	N	H	Hi	Hi
104109.85+001051.8	274	482	51913	1	1	0	0.00	2.250	19.03	-26.53	1913	974	...	H	H	Hi	Hi
104130.17+000118.8	274	179	51913	1	1	0	0.00	2.068	17.87	-27.51	672	705	0	H	H	HiLo?	Lo
104152.61-001102.1	274	159	51913	1	1	1	0.00	1.703	18.83	-26.14	1588	...	...	H	...	Hi	Hi
104233.86+010206.3	275	321	51910	1	1	1	0.00	2.123	18.39	-27.05	401	0	...	H	N	Hi	Hi
104841.02+000042.8	276	310	51909	1	1	0	0.00	2.022	18.75	-26.59	1176	840	...	H	H	Hi	Hi
105621.65+001243.5	276	551	51909	0	1	0	0.00	1.709	19.89	-25.10	333	...	...	H	...	Hi?	Hi
110041.19+003631.9	277	437	51908	1	1	1	0.00	2.017	18.18	-27.15	4687	3985	...	H	H	Hi	Hi
110533.17-005848.1	278	286	51900	1	1	1	0.00	1.742	18.34	-26.68	452	...	...	H	...	Hi?	Hi
110623.52-004326.0	278	251	51900	0	1	0	0.00	2.450	18.08	-27.65	4034	3828	...	H	H	HiZLo?	Lo
110728.45-005122.6	278	214	51900	0	1	0	0.00	1.730	18.94	-26.07	2815	...	663	H	...	Lo	Lo
110736.67+000329.4	278	271	51900	1	1	1	0.00	1.740	17.93	-27.09	123	...	...	H	...	Hi	Hi
110838.76-005533.7	278	123	51900	1	1	1	0.00	1.796	17.71	-27.38	0 <sup>e</sup>	...	...	N	...	Hi	Hi
112602.80+003418.3	281	432	51614	1	1	1	0.00	1.783	17.94	-27.14	1232	...	...	H	...	Hi	Hi
113212.92+010441.3	282	330	51658	1	1	1	0.00	2.250	19.07	-26.49	...	...	...	...	N	Fe?Loz	FeLo
113544.33+001118.6	282	510	51658	0	1	0	0.00	1.723	19.40	-25.61	3379	...	...	H	...	Hi	Hi
113621.05+005021.2	282	535	51658	1	1	0	0.00	3.439	17.85	-28.57	326	0	...	H	N	HiZ	Hi
114056.80-002329.9	283	315	51959	0	1	0	0.00	3.605	19.53	-26.99	1637	1861	...	H	H	HiZLo?	Lo
114534.51-004338.6	283	165	51959	1	1	1	7.52	1.748	18.92	-26.11	467	...	...	H	...	no?	Hi
115031.02-004403.1	284	261	51943	0	1	1	0.00	2.391	20.03	-25.65	1494	1390	...	H	H	HiZ	Hi
120657.01-002537.8	286	160	51999	1	1	1	0.00	2.005	19.03	-26.29	110	158	...	H	H	Hi	Hi
120834.84+002047.7	286	598	51999	0	1	0	0.00	2.708	18.21	-27.73	1646	195	...	H	H	HiZ	Hi
120957.19-002302.0	287	268	52023	1	1	1	0.00	1.861	18.59	-26.58	465	634	...	H	H	Hi	Hi
121323.94+010414.7	287	527	52023	0	0	1	21.54	2.836	20.10	-25.93	1968	939	...	H	H	HiZ	Hi

Table 1—Continued

SDSS Object (1)	Plate (2)	Fiber (3)	MJD (4)	Target <sup>a</sup>			$f_{20\text{cm}}$ (mJy) (8)	Redshift (9)	$i^*$ (10)	Dereddened $M_{i^*}$ (11)	C IV $BI^b$ (12)	C IV $BI^c$ (13)	Mg II $BI^b$ (14)	Classification <sup>d</sup>			Sub- sample (18)
				F (5)	E (6)	S (7)								1 (15)	2 (16)	3 (17)	
121549.81–003432.2	288	266	52000	1	1	0	0.00	2.705	17.13	–28.81	3598	4340	...	H	H	HiZ	Hi
121633.90+010732.8	287	604	52023	1	1	0	0.00	2.018	18.44	–26.89	2200	1191	...	H	H	Hi	Hi
121803.28+001236.8	287	624	52023	1	1	1	0.00	2.010	18.57	–26.75	269	30	...	H	H	no	Hi
122228.39–011011.0	288	2	52000	1	1	0	0.00	2.284	19.03	–26.55	678	0	...	H	N	HiZLo?	Lo
122848.21–010414.5	289	88	51990	1	1	1	29.36	2.654	17.80	–28.10	397	3	...	H	H	HiZ	Hi
122944.93+004253.0	289	573	51990	1	1	0	0.00	2.883	19.56	–26.51	1168	2168	...	H	H	HiZ	Hi
123056.58–005306.3	289	17	51990	1	1	0	0.00	2.162	18.72	–26.76	652	1301	...	H	H	Hi	Hi
123124.71+004719.1	289	610	51990	1	1	1	0.00	1.720	19.03	–25.97	3134	...	...	H	...	Hi	Hi
123525.27–003653.8	290	186	51941	1	1	1	0.00	1.950	19.03	–26.23	1076	631	...	H	H	Hi	Hi
123723.86–004210.0	290	145	51941	0	0	1	1.04	1.819	19.27	–25.85	2220	107	...	H	H	Hi	Hi
123824.90+001834.5	290	510	51941	1	1	1	0.00	2.154	19.06	–26.40	220	0	...	H	N	Hi	Hi
123947.61+002516.2	291	342	51928	0	1	0	0.00	1.869	19.44	–25.73	7299	5875	...	H	H	Hi	Hi
124551.45+010504.9	291	612	51928	1	1	1	0.00	2.808	17.88	–28.13	3512	3145	...	H	H	HiZ	Hi
124720.27–011343.1	292	292	51609	1	1	1	0.00	2.283	18.93	–26.66	336	0	...	H	N	HiZ	Hi
125241.55–002040.6	292	117	51609	0	1	1	0.00	2.898	18.47	–27.61	2524	1692	...	H	H	HiZLo?	Lo
130035.29–003928.4	293	104	51689	0	1	0	0.00	3.630	19.15	–27.38	853	778	...	H	H	HiZ	Hi
130058.13+010551.5	293	563	51689	1	1	1	0.00	1.903	18.97	–26.24	3848	3559	...	H	H	Hi	Hi
130136.13+000157.8	293	79	51689	1	1	0	0.00	1.784	17.41	–27.67	5898	...	...	H	...	Hi	Hi
130147.88–003817.3	293	65	51689	0	1	0	0.00	2.710	18.86	–27.08	2600	0	...	H	N	HiZ	Hi
130221.80–004638.1	293	12	51689	0	1	0	0.00	2.701	18.64	–27.30	1773	547	...	H	H	HiZ	Hi
130348.94+002010.4	294	390	51986	1	1	0	1.08	3.655	18.68	–27.87	1425	831	...	H	H	HiZLo?	Lo
130424.00–003757.2	294	264	51986	1	1	0	0.00	3.035	18.23	–27.95	1065	757	...	H	H	HiZ	Hi
130506.70+001908.5	294	393	51986	1	1	0	0.00	1.913	18.85	–26.37	509	673	...	H	H	Hi	Hi
131010.75–003007.2	294	72	51986	1	0	1	2.59	2.630	18.87	–27.01	4841	...	...	H	N	Loz	Lo
131333.01–005114.3	295	170	51985	1	1	0	0.00	2.949	19.11	–27.00	3794	2182	...	H	H	Loz	Lo
131714.21+010013.0	296	321	51665	1	1	0	0.00	2.691	18.06	–27.87	3240	2540	...	H	H	HiZ	Hi
131853.45+002211.4	296	386	51665	1	1	1	0.00	2.079	18.57	–26.82	1473	2226	...	H	H	Hi	Hi
132139.86–004151.9 <sup>§</sup>	296	147	51665	1	0	1	4.07	3.080	18.65	–27.56	2401	5158	...	H	H	FeLoZ	FeLo
132304.58–003856.5 <sup>§</sup>	296	67	51665	1	1	0	8.94	1.828	17.82	–27.31	287	273	...	H	H	Hi	Hi
132742.92+003532.6	297	504	51959	1	1	0	0.00	1.876	18.29	–26.89	671	63	...	H	H	Hi	Hi
134145.13–003631.0	299	172	51671	0	1	0	0.00	2.205	18.50	–27.02	870	1051	...	H	H	FeLo	FeLo
134544.55+002810.8	300	426	51666	1	1	1	0.00	2.516	18.48	–27.31	1510	2017	...	H	H	HiZ	Hi
134808.79+003723.2	300	461	51666	1	1	0	0.00	3.620	19.28	–27.25	1309	986	...	H	H	HiZ	Hi
135317.80–000501.3	300	33	51666	0	1	0	0.00	2.320	19.04	–26.58	9821	10190	...	H	H	Loz	Lo
135559.04–002413.6	301	267	51942	1	1	0	0.00	2.332	18.13	–27.50	1525	917	...	H	H	HiZ	Hi
135702.92+003824.4	301	414	51942	0	1	0	0.00	2.317	19.47	–26.15	415	618	...	H	H	HiZ	Hi
135721.77+005501.1	301	408	51942	1	1	1	2.75	2.001	17.98	–27.33	235	293	...	H	H	Hi?	Hi
140918.72+004824.3	302	535	51688	1	1	0	0.00	2.000	18.44	–26.87	1411	633	...	H	H	Hi	Hi
141332.35–004909.5	303	213	51615	1	1	0	0.00	4.140	19.19	–27.61	444	...	...	H	...	HiZ	Hi
142050.34–002553.1	304	123	51609	1	1	0	0.00	2.103	18.62	–26.80	3442	2016	...	H	H	HiZLo?	Lo
142232.38–003043.9	304	81	51609	0	1	0	0.00	2.711	19.28	–26.66	873	308	...	H	H	HiZ	Hi
142647.80+002739.9	305	476	51613	1	1	0	0.00	3.711	19.28	–27.30	197	126	...	H	H	HiZ	Hi
143022.47–002045.2	306	221	51637	0	1	0	0.00	2.544	19.35	–26.46	1957	2033	...	H	H	HiZ	Hi
143054.03–003627.3	306	225	51637	1	1	0	0.00	3.710	19.20	–27.37	9064	8737	...	H	H	HiZLo?	Lo
143307.40+003319.0	306	546	51637	0	1	1	0.00	2.745	19.11	–26.85	1832	517	...	H	H	HiZ	Hi
143641.24+001558.9	306	628	51637	1	1	1	0.00	1.867	18.33	–26.84	3890	2297	...	H	H	Hi	Hi
144256.86–004501.0	307	11	51663	1	1	0	0.00	2.226	18.17	–27.36	815	29	...	H	H	Hi	Hi
144959.97+003225.3	309	357	51994	1	1	0	0.00	1.709	18.94	–26.05	1530	...	...	H	...	Hi	Hi

Table 1—Continued

SDSS Object (1)	Plate (2)	Fiber (3)	MJD (4)	Target <sup>a</sup>			$f_{20\text{cm}}$ (mJy) (8)	Redshift (9)	$i^*$ (10)	Dereddened $M_{i^*}$ (11)	C IV $BI^b$ (12)	C IV $BI^c$ (13)	Mg II $BI^b$ (14)	Classification <sup>d</sup>			Sub- sample (18)	
				F (5)	E (6)	S (7)								1 (15)	2 (16)	3 (17)		
145045.42−004400.3	308	70	51662	1	1	1	0.00	2.078	18.27	−27.12	238	0	...	H	N	Hi	Hi	
145411.91+000341.5	309	472	51994	1	1	0	0.00	1.712	18.95	−26.04	1677	...	...	H	...	Hi	Hi	
145913.72+000215.8	310	305	51990	1	1	1	0.00	1.910	18.55	−26.67	356	266	...	H	H	Hi	Hi	
150033.52+003353.7	310	388	51990	1	1	0	0.00	2.451	18.02	−27.71	4257	3633	...	H	H	Hiz	Hi	
150114.37−005340.9	310	241	51990	1	1	0	0.00	3.279	19.48	−26.85	281	0	...	H	N	Hiz	Hi	
150206.66−003606.9	310	236	51990	1	1	0	0.00	9.87	2.202	18.49	−27.02	406	0	...	H	N	Hi	Hi
151636.79+002940.4 <sup>‡</sup>	312	434	51689	1	0	0	2.19	2.240	17.25	−28.29	4035	...	...	H	...	Lo	Lo	
152348.99−004701.8	313	213	51673	1	1	0	0.00	3.293	18.21	−28.13	2913	4333	...	H	H	Hiz	Hi	
152913.85−001013.8	313	32	51673	1	1	1	0.00	2.073	18.23	−27.16	209	0	...	H	N	Hi	Hi	
170056.85+602639.8	353	336	51703	1	1	1	...	2.125	18.51	−26.93	1400	1461	...	H	H	Hi	Hi	
170633.05+615715.1	351	555	51780	1	1	1	...	2.008	18.56	−26.76	171	28	...	H	H	Hi	Hi	
170720.18+613025.5	351	147	51780	1	1	1	...	1.744	18.74	−26.29	2655	...	...	H	...	Hi	Hi	
170903.06+594530.7	353	517	51703	1	1	1	...	1.708	18.64	−26.34	4936	...	...	H	...	Hi	Hi	
170931.00+630357.1	352	311	51694	0	1	0	...	2.402	17.25	−28.44	...	1232	...	...	H	Fe?Loz	FeLo	
170951.03+570313.7	355	310	51788	0	1	0	2.21	2.547	19.87	−25.94	528	0	...	H	N	Hiz	Hi	
171652.35+590200.2	353	63	51703	1	1	1	...	2.369	18.65	−27.01	620	716	...	H	H	Hiz	Hi	
171831.73+595309.3	353	624	51703	1	1	0	...	1.832	18.64	−26.49	1406	1423	...	H	H	Hi	Hi	
171944.76+554408.3	367	436	51997	1	1	0	0.00	3.886	19.69	−26.98	205	...	...	H	...	Hiz	Hi	
171949.92+532132.8	359	308	51821	1	1	1	0.00	1.777	18.00	−27.07	4903	...	...	H	...	Hi	Hi	
172001.31+621245.7	352	125	51694	1	1	1	...	1.762	18.70	−26.35	3290	...	...	H	...	Hi	Hi	
172012.40+545601.0	367	184	51997	1	1	0	0.00	2.099	18.24	−27.18	1249	44	...	H	H	Hi	Hi	
172310.22+573835.3	366	250	52017	0	0	1	0.00	1.780	20.00	−25.07	1817	...	...	H	...	Hi	Hi	
172341.09+555340.5 <sup>f</sup>	367	506	51997	1	1	1	0.00	2.113	18.47	−26.96	3497	...	...	H	N	FeLo	FeLo	
172413.28+571046.7	358	335	51818	1	1	0	0.00	2.815	17.88	−28.14	5806	6826	...	H	H	Hiz	Hi	
172656.65+535308.4	359	499	51821	0	1	0	0.00	2.905	19.61	−26.47	3770	3388	...	H	H	Hiz	Hi	
173049.10+585059.5 <sup>f</sup>	366	558	52017	0	0	1	...	1.980	20.76	−24.54	0 <sup>e</sup>	...	...	N	N	FeLo	FeLo	
173218.35+602014.0	354	69	51792	0	1	0	...	2.356	19.80	−25.86	534	104	...	H	H	Hiz	Hi	
173315.24+584814.3	366	593	52017	0	0	1	...	1.907	19.68	−25.54	374	179	...	H	H	Hi	Hi	
173722.98+572116.7	358	564	51818	1	1	0	0.00	1.944	19.00	−26.25	293	163	...	H	H	Hi	Hi	
173802.91+535047.2	360	132	51816	1	1	1	0.00	1.870	18.18	−27.00	2095	1305	...	H	H	Hi	Hi	
173911.52+565550.9	358	592	51818	1	1	0	0.00	1.772	18.90	−26.16	919	...	...	H	...	Hi	Hi	
173935.27+575201.7	358	605	51818	1	1	0	0.00	3.222	18.84	−27.45	473	42	...	H	H	Hiz	Hi	
232205.46+004550.9	383	388	51818	0	0	1	0.00	1.820	19.67	−25.45	222	28	...	H	H	Hi	Hi	
233934.42−002932.6	385	221	51877	0	1	0	0.00	2.010	19.70	−25.63	1242	2376	...	H	H	Hi	Hi	
234506.32+010135.5	385	617	51877	1	1	1	0.00	1.794	18.64	−26.45	2488	...	...	H	...	Hi	Hi	
234812.39+002939.5	386	388	51788	1	1	0	0.00	1.947	18.91	−26.35	5100	5289	1002	H	H	HiLo?	Lo	
235224.13−000951.0	386	180	51788	1	1	0	0.00	2.769	19.17	−26.81	1157	1556	...	H	H	Hiz	Hi	
235408.59−001615.1	386	106	51788	0	1	0	0.00	1.770	18.71	−26.35	10683	...	715	H	...	Lo	Lo	
235546.14−002342.9	386	28	51788	1	1	0	0.00	3.254	19.11	−27.20	7	12	...	H	H	no	Hi	
235628.96−003602.0	387	315	51791	1	1	0	0.00	2.940	18.61	−27.50	428	753	...	H	H	Hiz	Hi	
235859.46−002426.2	387	181	51791	1	1	1	0.00	1.757	17.98	−27.07	2199	...	...	H	...	Hi	Hi	

<sup>a</sup>Flags for final quasar target selection (F), EDR quasar target selection (E), and EDR serendipity target selection (S): 1 = selected, 0 = not selected.<sup>b</sup>Balnicity index computed using a fitted EDR composite spectrum as the continuum.<sup>c</sup>Balnicity index computed using a power law with Gaussian C IV emission line as the continuum.<sup>d</sup>Classification 1 is determined by the composite-fitting algorithm: H = HiBAL, N = nonBALQSO. Classification 2 is determined by the power law + Gaussian algorithm: H = HiBAL, N = nonBALQSO. Classification 3 lists the visual classifications as described in the text.<sup>e</sup>The BIs of these objects are formally zero (or unmeasured), but visual inspection suggests that the objects belong in this table. For SDSS0149−0114 and SDSS1132+0104 a small change in redshift would yield a positive BI. In the case of SDSS1730+5850, Hall et al. (2002) found a BI of >10900.<sup>f</sup>See also Hall et al. (2002).<sup>g</sup>See also Menou et al. (2001).<sup>h</sup>This quasar was selected for spectroscopic follow-up as a star.

Table 2. Supplementary SDSS EDR BALQSO Catalog

SDSS Object (1)	Plate (2)	Fiber (3)	MJD (4)	Target <sup>a</sup>			$f_{20\text{cm}}$ (mJy) (8)	Redshift (9)	$i^*$ (10)	Dereddened $M_{i^*}$ (11)	C IV $BI^b$ (12)	C IV $BI^c$ (13)	Mg II $BI^b$ (14)	Classification <sup>d</sup>			Sub- sample (18)
				F (5)	E (6)	S (7)								1 (15)	2 (16)	3 (17)	
002342.98+010242.8	390	610	51900	1	1	1	0.00	1.637	18.24	-26.66	...	...	...	...	...	Hi	Hi
010739.80-011042.5	396	41	51816	1	1	1	0.00	1.597	18.78	-26.06	...	...	...	...	...	Hi	Hi
010855.02-005747.2	397	296	51794	1	1	0	0.00	1.673	17.37	-27.58	...	...	...	...	...	Hi	Hi
011913.21+005115.8	398	453	51789	1	1	0	0.00	1.668	18.76	-26.18	...	...	...	...	...	Hi	Hi
012331.05+011314.6	399	367	51817	1	1	0	0.00	1.555	18.88	-25.91	...	...	...	...	...	Hi	Hi
012841.87-003317.2	399	26	51817	1	1	0	3.03	1.660	18.16	-26.77	...	...	...	...	...	Hi	Hi
013245.30-004610.0	400	252	51820	1	1	0	0.00	1.475	18.32	-26.36	...	...	194	...	...	Lo	Lo
014055.58+003908.4	401	437	51788	1	1	1	0.00	1.492	18.79	-25.91	...	...	...	...	...	Hi	Hi
020105.14+000617.9	403	593	51871	1	1	1	0.00	1.214	17.84	-26.43	...	...	0	...	...	Lo	Lo
025204.18+010710.3	410	321	51816	0	0	1	0.00	1.221	19.70	-24.58	...	...	4093	...	...	Lo	Lo
030000.56+004828.0 <sup>f</sup>	410	621	51816	1	1	0	0.00	0.892	16.38	-27.23	...	...	...	...	...	FeLo	FeLo
032246.82-005148.9	414	287	51869	1	1	1	...	1.680	18.87	-26.08	...	...	...	...	...	Hi	Hi
033818.29-003710.7	416	296	51811	0	0	1	...	1.582	19.42	-25.40	...	...	...	...	...	Hi	Hi
094302.93-001310.6	266	238	51630	1	1	1	0.00	1.590	18.38	-26.46	...	...	...	...	...	Hi	Hi
100021.83-010031.9	269	297	51910	1	1	0	0.00	1.656	18.95	-25.97	...	...	...	...	...	Hi	Hi
105352.86-005852.7	276	139	51909	1	1	1	24.01	1.572	17.50	-27.31	...	...	0	...	...	Lo	Lo
110826.31+003706.7	278	435	51900	1	1	0	0.00	4.410	19.74	-27.19	...	...	...	...	...	HiZ	Hi
111249.65+005310.1	278	619	51900	1	1	0	0.00	1.682	17.58	-27.38	...	...	...	...	...	Hi	Hi
113537.56+004130.1	282	540	51658	1	1	0	0.00	1.551	18.37	-26.41	...	...	...	...	...	Hi	Hi
114954.93+001255.2	284	353	51943	1	1	0	0.00	1.597	18.08	-26.77	...	...	...	...	...	Hi	Hi
115357.27-002754.0	285	302	51930	1	1	1	0.00	1.674	19.05	-25.90	...	...	...	...	...	Hi	Hi
115404.13+001419.5 <sup>g</sup>	284	516	51943	1	0	0	1.46	1.610	17.77	-27.10	...	...	0	...	...	Lo	Lo
120627.62+002335.3	286	499	51999	0	1	0	0.00	1.111	18.64	-25.44	...	...	...	...	...	FeLo	FeLo
120725.54+010154.8	286	570	51999	0	1	0	0.00	1.690	19.86	-25.10	...	...	...	...	...	Hi	Hi
121441.42-000137.9 <sup>f</sup>	287	514	52023	1	0	1	1.79	1.042	18.76	-25.19	...	...	2590	...	...	Lo	Lo
121701.50-002958.5	288	264	52000	1	1	0	0.00	1.608	19.05	-25.81	...	...	...	...	...	Hi	Hi
130208.26-003731.6 <sup>g</sup>	293	76	51689	1	1	0	11.24	1.672	17.60	-27.35	...	...	0	...	...	Lo	Lo
145857.57+002621.9	310	357	51990	1	1	1	0.00	1.554	18.79	-26.00	...	...	...	...	...	Hi	Hi
152839.31-002229.3	313	65	51673	1	1	1	0.00	1.593	18.33	-26.51	...	...	...	...	...	Hi	Hi
171124.23+593121.4	353	514	51703	1	1	0	...	1.491	18.72	-25.98	...	...	59	...	...	Lo	Lo
171330.98+610707.8	351	40	51780	1	1	1	...	1.685	18.78	-26.18	...	...	...	...	...	Hi	Hi
171430.12+561523.9	367	338	51997	1	1	0	0.00	1.678	18.51	-26.44	...	...	...	...	...	Hi	Hi
172308.15+524455.4	359	207	51821	0 <sup>e</sup>	0	0	2.07	1.815	17.07	-28.05	0	0	...	N	N	Hi?	Hi
172630.05+615208.3	354	529	51792	0	0	1	...	1.591	19.83	-25.00	...	...	...	...	...	Hi	Hi
172718.39+585227.9	366	507	52017	1	1	1	0.00	1.550	18.65	-26.14	...	...	0	...	...	Lo	Lo
173221.93+604854.9	354	638	51792	1	1	0	...	1.540	18.12	-26.65	...	...	...	...	...	Hi	Hi
173523.03+554611.1	360	414	51816	1	1	0	0.00	1.588	17.42	-27.41	...	...	...	...	...	Hi	Hi
235238.08+010552.4	386	524	51788	0	1	0	0.00	2.156	17.23	-28.23	0	0	...	N	N	Hi	Hi
235253.51-002850.4	386	167	51788	1	1	1	0.00	1.628	17.87	-27.02	...	...	54	...	...	HiLo?	Lo

<sup>a</sup>Flags for final quasar target selection (F), EDR quasar target selection (E), and EDR serendipity target selection (S): 1 = selected, 0 = not selected.

<sup>b</sup>Balnicity index computed using a fitted EDR composite spectrum as the continuum.

<sup>c</sup>Balnicity index computed using a power law with Gaussian C IV emission line as the continuum.

<sup>d</sup>Classification 1 is determined by the composite-fitting algorithm: H = HiBAL, N = nonBALQSO. Classification 2 is determined by the power law + Gaussian algorithm: H = HiBAL, N = nonBALQSO. Classification 3 lists the visual classifications as described in the text.

<sup>e</sup>This quasar was selected for spectroscopic follow-up as a galaxy.

<sup>f</sup>See also Hall et al. (2002).

<sup>g</sup>See also Menou et al. (2001).